

This is a non-peer-reviewed preprint submitted to EarthArXiv.

Enzyme-Mediated Multiphase Precipitation (EMMP): An Innovative Strategy for Ecotoxic
Metal Immobilization in Aqueous Systems

Dickinson, Heloisa^a ; MacDonald, John^a ; Toney, Jaime L.^a

^aCollege of Sciences and Engineering, School of Geographical and Earth Sciences,
University of Glasgow

Corresponding author: h.dickinson.2@research.gla.ac.uk

Co-authors: Jaime.Toney@glasgow.ac.uk

John.MacDonald.3@glasgow.ac.uk

v.1.2.

Enzyme-Mediated Multiphase Precipitation (EMMP):
An Innovative Strategy for Ecotoxic Metal Immobilization

in Aqueous Systems

Dickinson, Heloisa^a; MacDonald, John^a; Toney, Jaime L.^a

^a *College of Sciences and Engineering, School of Geographical and Earth Sciences, University of Glasgow*

Abstract

Ecotoxic metal contamination in wastewater and soil poses a critical environmental challenge due to its persistence, toxicity, and bioaccumulation potential. While conventional biogeotechnical methods like Enzyme-Induced Carbonate Precipitation (EICP) and Microbial Induced Carbonate Precipitation (MICP) have shown promise for metal immobilisation, their application is limited by excessive ammonium byproduct generation. In this paper, we present Enzyme-Mediated Multiphase Precipitation (EMMP), a novel approach that significantly reduces ammonium production while utilising waste-derived materials (i.e., soybean crude urease extract, bone meal and urea) to achieve simultaneous precipitation of metal-magnesium ammonium phosphates, carbonates, and calcium phosphates. We evaluated EMMP's effectiveness in removing nine metals (As, Cd, Co, Cr, Cu, Li, Ni, Pb, Zn) at three concentrations (2 mM, 5 mM, 20 mM). The process achieved removal efficiencies exceeding 95% for Pb, Cd, and Zn and 80% for Co, Ni, and Li through combined mechanisms of direct precipitation, co-precipitation, surface adsorption, and biomolecule-mediated interactions. Crystallographic analysis revealed calcite and struvite as primary mineral phases with distinct metal-dependent morphological variations. Relative to control conditions (defined as 100% ammonium production), EMMP reduced ammonium generation to below 5% for Cr, Cu, Pb, and As, to 20-45% for Ni, Co, and Cd, and maintained levels at 78-82% for Li and Zn. By integrating waste-derived materials and minimising ammonium generation, EMMP demonstrates an efficient, sustainable approach for metal remediation in aqueous environments, aligning with circular economy principles.

1. Introduction

Anthropogenic ecotoxic metals (EMs) contamination in water and soil is a major environmental issue in many urban areas. This increased concentration of EMs in soil and groundwater is not merely a significant public health matter but is also responsible for hindering ecosystem services such as nutrient cycling, soil fertility and carbon sequestration that are indispensable in a liveable city [1]. Sustainable land-use practices, pollution remediation and prevention, and conservation efforts that consider soil and groundwater are essential for maintaining the health and functionality of these vital ecosystems. Protecting soil and groundwater ecosystem services is necessary to guarantee water and food security, ecological health, and resilience to environmental change [2].

Given the need for effective strategies to mitigate EMs contamination and restore ecosystem services, innovative biogeotechnical approaches have been explored for wastewater and soil remediation and stabilisation. Among these, Microbial Induced Carbonate Precipitation

(MICP) and Enzyme Induced Carbonate Precipitation (EICP) have gained attention as sustainable techniques with the potential to immobilise EMs and simultaneously sequester carbon dioxide from the atmosphere or waste sources [3][4][5][6][7]. MICP and EICP rely on urease enzymes produced by ureolytic microorganisms or directly extracted from plants or organisms to catalyse the hydrolysis of urea into ammonia and carbon dioxide, leading to the precipitation of calcium carbonate (CaCO_3) [8][9]. The enzymatic and microbial processes that induce carbonate precipitation can also be leveraged to immobilise and sequester contaminants in wastewater and the soil matrix [10][11]. Both techniques proved to be efficient in immobilising inorganic contaminants predominantly through mechanisms of direct precipitation, co-precipitation, adsorption and surface complexation in distinct environmental contexts, such as groundwater and wastewater [12][13][14], soil improvement and erosion control [15][16][17][18] and mining waste [19][20]. However, the ureolytic precipitation of carbonates generates substantial amounts of ammonium, which transforms into ammonia through pH-dependent equilibrium and can lead to environmental issues such as eutrophication, bio-toxicity, soil acidification, and formation of inorganic secondary particulate matter [21][22].

Several methods have been proposed for the remediation of ammonium, such as ion exchange, struvite ($(\text{NH}_4)\text{MgPO}_4 \cdot 6\text{H}_2\text{O}$) precipitation, nitrification/denitrification, and adsorption [23][24][25][26][27]. Combining methods can often yield the best results, leveraging the strengths of each method to effectively manage and remove ammonium byproducts from MICP and EICP processes applied in soil and water [24]. A significant challenge lies in the fact that once released into the environment, ammonium tends to be chemically adsorbed in the clay minerals or organic matter of the soils; it can also be dispersed through water systems or be transformed into gas ammonia, depending on the pH of the media. Managing and mitigating the dispersion of ammonium [NH_4^+] and its transformation into ammonia [NH_3] in the environment requires a strategic approach that involves containment and treatment. Although proven effective for ammonium remediation, the cited methods - combined or individually - constitute independent secondary treatment strategies that introduce additional steps to the initial remediation process, increasing both process complexity and operational costs. Selecting the appropriate method, or combination of methods, depends on factors such as the scale of the project, local environmental conditions, and specific site requirements while evaluating their economic feasibility and environmental trade-offs through Life Cycle Assessment (LCA) can provide crucial insights into their long-term sustainability and cost-effectiveness.

In light of these challenges, alternative approaches that address soil remediation and ammonium management in a single process have emerged. Phosphate precipitation mediated by enzymes or microbial activity is a dynamic and potent method for remediating environments polluted by heavy metals and radionuclides, with reported remediation rates above 95% [28][29]. The precipitation of phosphates induced by ureolytic processes has two important additional benefits when compared to EICP and MICP: 1) some of the precipitated phosphate phases like struvite and brushite can sequester the ammonium byproduct via mechanisms of precipitation and adsorption, and 2) due to general lower solubility, phosphates demonstrate better performance in stabilising heavy metals compared to carbonates, particularly for Pb and Zn, remaining immobilised in a broader range of pH, even in more acidic conditions [28].

In this study, we investigated the efficiency of Enzyme-Mediated Multiphase Precipitation (EMMP), a novel technique inspired by EICP and phosphate precipitation techniques that generate less ammonium byproduct than conventional EICP methods during EMs immobilisation. EMMP uses a single-stage process involving plant-derived urease crude extract, bone meal, and urea to precipitate carbonates and metal-magnesium ammonium phosphates (M-struvite species) as the main mineral phases.

We implemented a “waste-to-resource” strategy by substituting commercial-grade materials with locally sourced residual biomaterials, aiming to reduce environmental impact and increase process sustainability. By examining how waste-derived inputs influence mineralisation pathways, we aim to demonstrate their viability in achieving comparable outcomes to conventional materials, while improving the sustainability and mechanistic transparency of the EMMP process. The method’s effectiveness was evaluated based on its capacity to immobilise nine environmentally relevant metals—Cd, Co, Cu, Cr, As, Li, Ni, Pb, and Zn—while simultaneously sequestering ammonium. In addition to quantifying performance, this research tries to shed some light onto the underlying immobilisation pathways, including direct and indirect precipitation mechanisms and biomolecular interactions with metals.

To assess EMMP performance, we conducted test tube experiments across three concentrations of each EM species. Single Crystal X-ray Diffraction (SC-XRD), Powder X-ray Diffraction (PXRD), and Scanning Electron Microscopy with Energy Dispersive X-ray Spectroscopy (SEM-EDS) were employed to characterise mineral phases and crystal structures. In parallel, Ion Chromatography (IC) and Inductively Coupled Plasma-Optical Emission Spectrometry (ICP-OES) were used to determine the chemical composition of solutions before and after treatment.

1.1. Theoretical framework

The Enzyme-Mediated Multiphase Precipitation (EMMP) method is driven by a precipitation solution containing crude urease extract, bone meal, and urea, which induces the formation of mineral phases. The immobilization of EMs through EMMP in aqueous solutions occurs through multiple pathways involving mineral precipitation, functional group binding, electrostatic/ion exchange interactions, and adsorption mechanisms that combined enhance the immobilization of toxic metal ions, reducing their mobility and bioavailability. These pathways do not act independently; they operate within a broader biogeochemical framework that integrates biocatalysis, geochemical transformations, and organic-mineral interactions. This integrated perspective, referred to as biogeochemical trapping, describes the collective set of biological, chemical, and geological interactions that may contribute to metal immobilization through biogeochemical methods in aqueous environments, providing an efficient pathway for metal immobilization beyond conventional physicochemical mechanisms that rely on a single immobilization route. These processes are further detailed in the sections below.

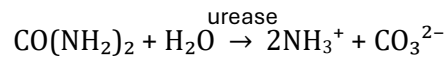
1.1.1. Mineral Precipitation

Mineral precipitation via EMMP primarily occurs through urease-driven biochemical reactions that facilitate carbonate and phosphate formation. The cementation solution provides

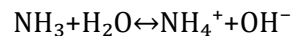
the necessary enzymatic activity, biomolecules, and ions that drive the process. Factors such as pH, ionic composition, and the presence of organic and inorganic molecules further influence the stability, transformation, and evolution of the resulting mineral phases. In addition to enzyme-mediated processes, direct precipitation can also take place when metal ions react with available carbonate or phosphate species in solution, leading to the formation of insoluble mineral phases.

1.1.1.1. Urease-Driven Carbonate and Phosphate Precipitation

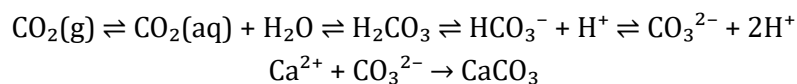
The core of EMMP mineral precipitation should begin with the urease-catalysed hydrolysis of urea [30]:



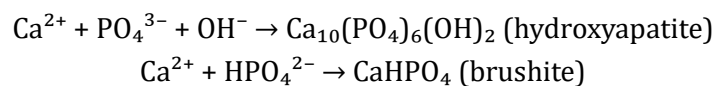
This reaction generates carbonate species, which contribute to mineral formation, while simultaneously increasing the system's pH due to ammonium and hydroxide ion production. Initially, under acidic conditions (pH 3.85–4.11), most ammonia (NH_3) is protonated into ammonium (NH_4^+), limiting the immediate rise in pH. However, as hydrolysis progresses and NH_3 accumulates, it reacts with water to form hydroxide ions (OH^-), which gradually increase the pH and favour carbonate formation and subsequent mineral precipitation.



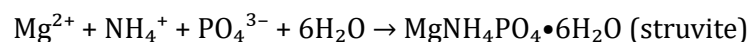
As the pH continues to rise, the system transitions from acidic to alkaline conditions allows the participation of atmospheric CO_2 in the carbonate precipitation process through equilibrium reactions:



Simultaneously, phosphate ions present in solution participate in multiple precipitation pathways forming calcium phosphate compounds [31]:



Additionally, the presence of magnesium and ammonium enables the formation of struvite-family minerals:



1.1.1.2. Direct Bone-meal-Induced Mineral Precipitation

Bone meal extract serves as a rich source of calcium (Ca^{2+}) and phosphate (PO_4^{3-}) ions, which facilitate hydroxyapatite ($\text{Ca}_{10}(\text{PO}_4)_6(\text{OH})_2$) precipitation and other metal-phosphate mineral formations, depending on metal availability, pH conditions, and solution chemistry. Heavy metals such as Pb^{2+} , Cu^{2+} , and Zn^{2+} can either substitute for calcium within the hydroxyapatite structure or form separate phosphate precipitates [33][34]. Phosphate-based minerals such as pyromorphite ($\text{Pb}_5(\text{PO}_4)_3\text{Cl}$), copper phosphate ($\text{Cu}_3(\text{PO}_4)_2$), and zinc phosphate ($\text{Zn}_3(\text{PO}_4)_2$) may also form, with amorphous calcium phosphate (ACP) serving as an intermediate phase [35]. This process is particularly effective for lead (Pb^{2+}), which preferentially forms pyromorphite ($\text{Pb}_5(\text{PO}_4)_3\text{Cl}$), a highly stable phase under a wide range of environmental conditions [35][36]. Furthermore, competitive ions such as carbonate and sulphate can influence precipitation pathways and the phase stability of the resulting mineral products.

1.1.2. Functional group binding

EMs can also be immobilized by interacting with specific functional groups present in organic molecules derived from soybean and bone meal, including proteins, peptides, polysaccharides, and lipids. These interactions rely on chelation, complexation, and covalent bonding, which contribute to metal immobilization at a molecular level [37][38][39][40]. In addition to these biomolecules, bone meal contains collagen, phosphoproteins, and glycoproteins, which provide additional functional groups for metal binding, enhancing sequestration pathways [41].

Biomolecules containing sulfhydryl (-SH) groups exhibit a strong affinity for soft metal ions such as Pb^{2+} , Cd^{2+} , and Hg^{2+} , forming highly stable metal-thiolate complexes [43]. Sulphur-containing amino acids in soybean proteins, particularly cysteine and methionine, are known to bind heavy metals through thiol-metal interactions, forming stable thiolate complexes [37]. Although specific studies on soybean proteins are still emerging, the role of sulphur-containing functional groups in metal binding has been extensively reported for carbon-based adsorbents. Yang et al. [44] demonstrated that the introduction of sulphur functional groups (e.g., thiol, sulfonic) onto activated carbon, graphene oxide, and carbon nanotubes significantly enhances their capacity to adsorb metals such as $\text{Pb}(\text{II})$, $\text{Cd}(\text{II})$, and $\text{Hg}(\text{II})$ through surface complexation and precipitation mechanisms. Bulgariu et al. [45] did not investigate molecular-level mechanisms, but their study confirmed the high sorption capacity of alkaline-treated soybean waste biomass for Pb^{2+} , Cd^{2+} , and Zn^{2+} , suggesting the presence of diverse functional groups that facilitate metal retention.

Carboxyl (-COOH) functional groups, commonly found in proteins, peptides, and organic acids, contribute to metal sequestration by forming stable coordination complexes with metal ions [37]. This process is particularly relevant for Pb^{2+} , Zn^{2+} , Cu^{2+} , and Ni^{2+} , where carboxyl groups facilitate metal binding through ligand exchange, stabilizing metal-organic interactions and reducing solubility in solution.

Amino groups (-NH₂), abundant in peptides and proteins, also play a crucial role in metal coordination but through distinct mechanisms. These groups function as electron donors, forming coordination bonds that stabilize metal ions in solution and facilitate their retention in organic structures [44][46]. This interaction is particularly relevant for Cu^{2+} , Ni^{2+} , and Zn^{2+} , as amine

ligands can modulate metal speciation, influence redox behaviour, and contribute to the stabilization of metal-protein complexes.

The efficiency of metal binding varies depending on the specific biomolecular interactions. Studies indicate that proteinaceous components of crude urease extracts exhibit a preferential affinity in the order of $Zn > Ni > Cr$, likely due to differences in coordination chemistry and molecular conformation [37][47]. Similarly, proteins and phosphoproteins from the bonemeal solution provide additional metal-binding sites, potentially altering selectivity patterns and influencing sequestration pathways. This suggests that biomolecular interactions not only aid in metal sequestration but may also affect the preferential incorporation of certain metals into mineral phases.

1.1.3. Electrostatic Attraction

Adsorption is another key pathway for metal immobilization in enzyme-mediated systems, involving both biomolecular surfaces (proteins, polysaccharides, phosphoproteins) and mineral phases ($CaCO_3$, hydroxyapatite, and other precipitates). Physisorption occurs through weak van der Waals forces and electrostatic attraction, leading to reversible metal attachment onto these surfaces, whereas chemisorption involves stronger covalent or ionic bonding with functional groups such as carboxyl ($-COOH$), amine ($-NH_2$), and sulfhydryl ($-SH$) [37]. Moreover, chemisorption may involve charge transfer mechanisms, where metal ions share or transfer electrons with biomolecular ligands or mineral surfaces, forming stable coordination complexes.

Surface complexation further contributes to adsorption, as metal ions displace water molecules in their hydration shells and directly bond with functional groups via ligand exchange reactions [49][50]. This mechanism is particularly relevant for divalent metal cations such as Zn^{2+} , Ni^{2+} , and Cu^{2+} , which exhibit a strong affinity for carboxyl and amine groups on biomolecules, as well as reactive sites on mineral surfaces [51].

The efficiency of adsorption depends on metal competition for binding sites, with sequestration capacity varying under different environmental conditions. Organic molecules, including proteins and polysaccharides in crude urease extracts, as well as phosphoproteins, collagen, and bone-derived glycoproteins from bonemeal, modify the surface charge and hydrophilicity of both biomolecules and mineral precipitates, affecting their adsorption affinity. Studies suggest that metals with higher charge densities, such as Zn^{2+} and Ni^{2+} , tend to form more stable inner-sphere complexes, whereas larger, more electropositive ions exhibit weaker interactions.

1.1.4. Evolution of Mineral Phases

Organic molecules in crude urease extracts and bone meal play a crucial role in mineral nucleation and growth, acting as nucleation sites and influencing mineral morphology. Proteins and polysaccharides can stabilize amorphous or metastable phases before they transition into more thermodynamically stable minerals [52]. Biomolecule-mediated interactions further influence mineralization by introducing functional groups ($-COOH$, $-NH_2$, $-OH$) that modify crystal

formation and stabilization [53] [54]. These biomolecules can function as nucleation sites, guiding the precipitation of phosphates and carbonates into structurally stable [55][56].

Once precipitated, mineral phases undergo transformations due to thermodynamic and kinetic conditions. Some minerals crystallize directly into their stable forms, while others evolve through dissolution-reprecipitation, Ostwald ripening, or solid-state transitions [57]. For example, calcium carbonate may initially precipitate as vaterite or aragonite before transforming into the more thermodynamically stable calcite phase [58]. Similarly, amorphous calcium phosphate (ACP) frequently serves as a precursor to hydroxyapatite, with its transformation influenced by pH, ionic strength, and biomolecular interactions [59][60].

Finally, carbonate and phosphate systems interact, leading to the formation of carbonate-substituted apatite or the conversion of calcite into phosphate phases in phosphate-rich conditions. This transition has been observed in biomineralization and hydrothermal studies, where calcium carbonate acts as a precursor for hydroxyapatite via dissolution-reprecipitation mechanisms [61].

2. Material and Methods

2.1. Materials

We investigated mineral precipitation using synthetic solutions individually spiked with one of nine EMs—As, Cd, Co, Cr, Cu, Li, Ni, Pb, and Zn—at three initial concentrations corresponding to treatment levels: T1 (2 mM), T2 (5 mM), and T3 (20 mM). The experimental setup included a crude urease extract derived from soybean (*Glycine max*), powdered urea added to the EM solution to achieve a final concentration of 1 M, and a bonemeal solution serving as a source of Ca, P, Mg, and K. Bonemeal (Westland) was obtained from a local garden centre, and soybeans (Jalpur) were purchased from a local supermarket.

Urea (98% purity) and the metal reagents—CdCl₂, CoCl₂, Cr₂(SO₄)₃·xH₂O, CuCl₂, AsCl₃, LiCl, NiCl₂, PbCl₂, and ZnCl₂—were purchased from Sigma-Aldrich. All metal salts were anhydrous, in powder form, and had a trace metals basis purity of ≥99.995%. Deionised water with a resistivity of 18.2 MΩ·cm, produced by the Milli-Q Ultrapure and Pure Water Purification System in the Environmental Biogeochemistry laboratory at the University of Glasgow, was used to prepare all solutions.

2.1.1. Bone meal solution preparation

The bonemeal solution (BMS) was prepared with slight modifications to the method proposed by Gowthaman [31]. Specifically, 50 grams of bonemeal were added to a beaker containing 250 mL of deionized water and 60 mL of 1 M hydrochloric acid. The mixture was stirred for 2–3 minutes, left to rest overnight, and filtered the following day using Grade 2 laboratory filter paper. The composition of the resulting solution was analysed using ICP-OES, with the concentrations of the primary components presented in Table 1. Additionally, the pH and

electrical conductivity were measured using a YSI sensor and normalized to a standard temperature of 25°C.

Table 1

Electroconductivity (EC), pH and average (N = 7) concentration of Mg, Ca, K and P in the bonemeal solution.

Ca (ppm)	K (ppm)	Mg (ppm)	P (ppm)	pH	EC (uS/cm)
14577.00 ± 132.5	266.50 ± 6.37	316.50 ± 8.41	6349.00 ± 77.59	3.35 ± 0.31	167 ± 5.00

2.1.2. Preliminary Optimization of Soybean Concentration and Operational Parameters

The optimization of soybean concentration and operational parameters was evaluated through direct mass measurement of precipitates. Soybean extracts were prepared at concentrations of 20, 40, 60, 80, and 100 g/L in deionized water, each assessed with urea concentrations of 0.5, 0.75, and 1.0 M, while bone meal composition remained constant (Table 1). The experimental design encompassed both concentration variations and mixing ratio permutations, with each combination assessed in triplicate to ensure statistical validity. Quantitative analysis revealed that an 80 g/L soybean extract combined with 1.0 M urea solution and with bone meal solution in a ratio of 3:3:1, respectively, yielded the maximum precipitate mass under controlled laboratory conditions. Complete experimental protocols are provided in the Supplementary Materials.

2.1.3. Crude urease extract preparation

The crude urease extract (CUE) was prepared by combining 80 grams of soybeans with deionised water in a beaker until the total volume reached 1 L. The mixture was left overnight, then processed using a Fridja f1900 self-feeding cold press masticating juicer (1 L capacity, 250 W motor) to separate the solid and liquid components. The resulting liquid was mixed with calcium carbonate (CaCO₃) to achieve an approximate concentration of 0.06 M, facilitating the removal of excess protein. The mixture was left to decant for 2 hours, after which the supernatant was collected, centrifuged at 3700 rpm for 15 minutes at 4°C, and filtered using laboratory-grade paper filter (Grade 2). Enzyme activity was measured using the method proposed by Whiffin [62], yielding an activity of 6.2 ± 0.7 mM urea·min⁻¹. A summary of the functions and proposed sources of the materials used in the EMMP mineralisation solution is provided in Table 2.

Table 2

Materials used in the EMMP mineralisation solution, their functions and proposed waste sources.

Material	Function	Waste Source of the Product
Soybean Crude Urease Extract (CUE)	Catalyser of urea hydrolysis	We propose using soybeans as a source of urease, given that they are the 5 th most cultivated crop worldwide, with a significant global presence [2]. Annually, copious quantities of soybeans are discarded due to quality control issues, presenting an opportunity for their utilisation as a urease source. Additionally, soy-based

		food industries could provide another viable source of soybean urease.
Urea	Substrate for urease; its hydrolysis catalysed by urease produces carbonate ions (CO_3^{2-}) and ammonium (NH_4^+).	Urea is a common waste in water treatment centres and can be sourced from animal and human urine.
Bonemeal solution (BMS)	Source of P, Mg and Ca	Bonemeal is a common food waste product derived from discarded fish and mammal carcasses.

2.2. Experimental procedure

To evaluate the immobilization of EMs using Enzyme-Mediated Mineral Precipitation (EMMP), a series of experiments were conducted using a cementation solution (CS). This solution was prepared by mixing urea, crude urease extract (CUE), and bone meal solution (BMS) in a 3:3:1 ratio, as determined by preliminary tests. CS was created by combining 110 mL of CUE, 110 mL of EMs solution in the desired concentration with added urea to achieve a 1M solution, and 36 mL of BMS. The mixture was then distributed into five 50 mL Falcon test tubes incubated at 25 °C for 72 hours until the end of the precipitation process, then left curing for 4 days. Afterwards, the precipitated content was washed with deionised water, filtered using Grade 2 filter paper, and placed in an oven at 37 °C for 24 hours. Aliquots of the residual liquid were collected for chemical composition analysis and for pH and electroconductivity measurements. The dried precipitates were stored in small plastic containers for further characterisation.

2.3. Assessment of the immobilisation of EMs and ammonium production

The residual liquid generated during precipitation experiments was analysed to assess its efficiency in immobilising EMs and ammonium production. Residual liquid aliquots were first filtered using Grade 2 filter paper (Whatman) to remove solid matter. An aliquot of the residual liquid was filtered with 0.45 µm pore size syringe filters and used for colorimetric ammonium determination via the salicylate method using a SEAL AutoAnalyzer (AA3). To further evaluate pH and electrical conductivity (EC) measurements were conducted using a YSI ProDSS Multiparameter Probe. The measurements were recalibrated to 25 °C to ensure consistency in interpretation.

Nitric acid (HNO_3) was added to an aliquot of the filtered solution to achieve a final concentration of 2% (v/v). Subsequently, the solution was analysed using Inductively Coupled Plasma Optical Emission Spectroscopy (ICP-OES) (Thermo Scientific iCAP 7000), enabling the quantification of the final concentrations of the nine EMs.

2.4. Characterization of the precipitates

For micromorphological studies, the precipitates formed during the experiments were separated into two fractions using a sieving system: one containing crystals larger than 1 mm and the other containing crystals smaller than 1 mm. The larger fraction was examined using a Zeiss

stereomicroscope to observe their habit, colour, and size, providing a qualitative understanding of the macroscale features of the precipitates.

The smaller fraction, containing crystals below 1 mm, was analysed using scanning electron microscopy (SEM) to study their morphology and size in greater detail. Energy Dispersive X-ray Spectroscopy (EDS) was employed alongside SEM to verify the elemental composition of the precipitates and to correlate the observed morphologies with the two main mineral phases—calcite (CaCO_3) and struvite ($\text{MgNH}_4\text{PO}_4 \cdot 6\text{H}_2\text{O}$).

In addition, Powder X-ray Diffraction was performed using the entire precipitate powder, rather than a fraction, to identify the phases present and quantify the relative proportions of calcite and struvite for each element and treatment.

Details of methodological procedures are provided in the Supplementary Materials.

3. Results

3.1. System response parameters

This section presents four key system response parameters measured at the end of the curing period of the EMMP experiments. These parameters - pH, mass of precipitates, ammonium production, and metal removal efficiency - reflect the chemical and mineralogical responses of the system under the experimental conditions. All reported values represent the average of five experimental replicates, except for the ammonium production which refers to a single measurement. Figure 1 presents pH and precipitate mass, while Figure 2 shows metal removal efficiency and ammonium production. Together, these figures illustrate distinct patterns for each metal across three treatments (T1–T3), corresponding to EMs concentrations of 2 mM (T1), 5 mM (T2), and 20 mM (T3) in the EMS solution. The control sample (without EMs) produced 12,877 ppm for ammonium production, compared to a theoretical maximum of 14,757 ppm, providing a baseline for comparing metal-specific responses.

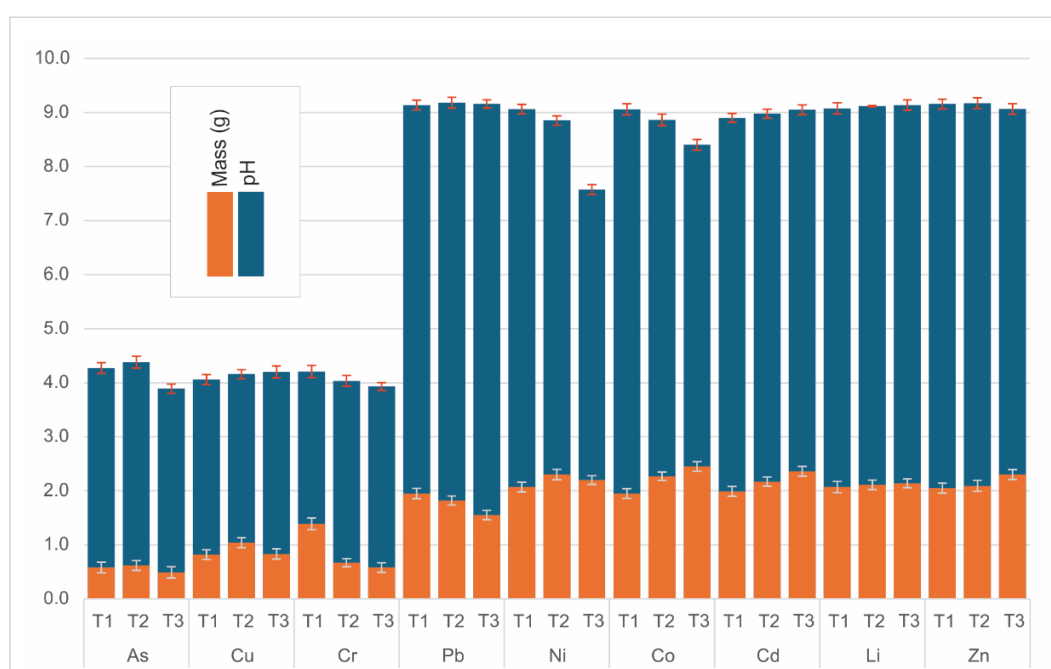


Figure 1. The figure presents pH levels (blue bars) and precipitate mass (orange bars) obtained at the end of the EMMP experiment across different elements and three treatments (T1 = 2mM, T2 = 5mM, T3 = 20mM). The X-axis shows treatment-element combinations, with both parameters plotted on the same Y-axis. Values represent averages of five replicates (N = 5).

3.1.1. pH

The initial pH of the liquid ranged from 3.85 to 4.11 ± 0.1 for all metals. Based on their characteristic pH ranges in the residual liquid, the metals segregated into two distinct domains - an acidic domain (pH 3.89-4.38) and an alkaline domain (pH >7.50) (Figure 1).

In the acidic domain, arsenic showed a slight increase in pH from 4.07 in T1 to 4.38 in T2, followed by a significant drop to 3.89 in T3. Copper displayed a steady linear pH increase across treatments, from 4.07 in T1 to 4.18 in T3. Chromium experienced a consistent drop in pH, from 4.21 in T1 to 3.93 in T3.

In the alkaline group, consisting of Pb, Ni, Co, Cd, Li, and Zn, varied pH behaviours were observed. Lead maintained a highly stable alkaline pH across treatments, ranging from 9.14 in T1 to 9.16 in T3. Nickel exhibited a decreasing pH trend, from 9.06 in T1 to 7.57 in T3. Similarly, cobalt showed a steady pH decline, from 9.06 in T1 to 8.40 in T3. Cadmium, lithium, and zinc demonstrated minimal pH variations, maintaining consistent alkaline conditions. Cadmium ranged between 8.90 and 9.05, while lithium and zinc maintained a narrow range of 9.08–9.14 and 9.16–9.07, respectively.

3.1.2. Mass of precipitates

Precipitate mass values are reported in grams. Over the treatment period, four metals—cobalt, cadmium, zinc, and lithium—exhibited an overall linear increase in mass with rising metal concentration (Figure 1) from T1 to T3. Cobalt increased from 1.95 g to 2.45 g, while cadmium rose from 1.99 g to 2.36 g. Zinc and lithium showed more moderate gains, with zinc increasing from 2.05 g to 2.30 g and lithium from 2.07 g to 2.14 g.

In contrast, two metals, lead and chromium, experienced consistent linear declines as metal concentrations increased. Lead decreased from 1.95 g to 1.55 g, whereas chromium exhibited a more pronounced drop from 1.39 g to 0.58 g.

The remaining three metals—copper, nickel, and arsenic—peaked at T2 before declining in T3. Copper rose from 0.82 g to 1.04 g before decreasing to 0.83 g, while arsenic increased from 0.58 g to 0.62 g before falling to 0.49 g. Nickel reached its highest mass at 2.30 g in T2, then slightly decreased to 2.20 g in T3, still exceeding its initial 2.07 g.

3.1.3. Ammonium production

The values presented in Figure 2 represent the percentage of ammonium produced relative to the control, with 100% corresponding to the average ammonium concentration measured in control samples (12,877 ppm). According to observed values (Figure 2), ammonium production fell into three distinct ranges: 1.73–4.31% (low), 16.56–48.97% (medium), and 69.47–85.97% (high).

In the low range, arsenic, chromium, copper, and lead showed varying patterns. Arsenic peaked at 4.19% in T2, between values of 3.46% and 2.80% in T1 and T3. Chromium declined steadily from 2.33% to 1.73%, while copper maintained stable values between 2.25–2.33%. Lead showed the highest initial value in this range at 4.31%, before decreasing to 2.02% by T3.

In the medium range, nickel and cobalt showed linear parallel declines from T1 to T3 — nickel from 24.94% to 16.56%, and cobalt from 32.90% to 17.71%. In contrast, cadmium increased steadily from 39.16% to 48.97% across treatments.

In the high range, lithium and zinc maintained the highest concentrations throughout. Lithium increased from 79.63% to 85.97% in T2, before stabilising at 85.80%. Zinc showed a gradual linear decline from 80.42% to 69.47% across treatments.

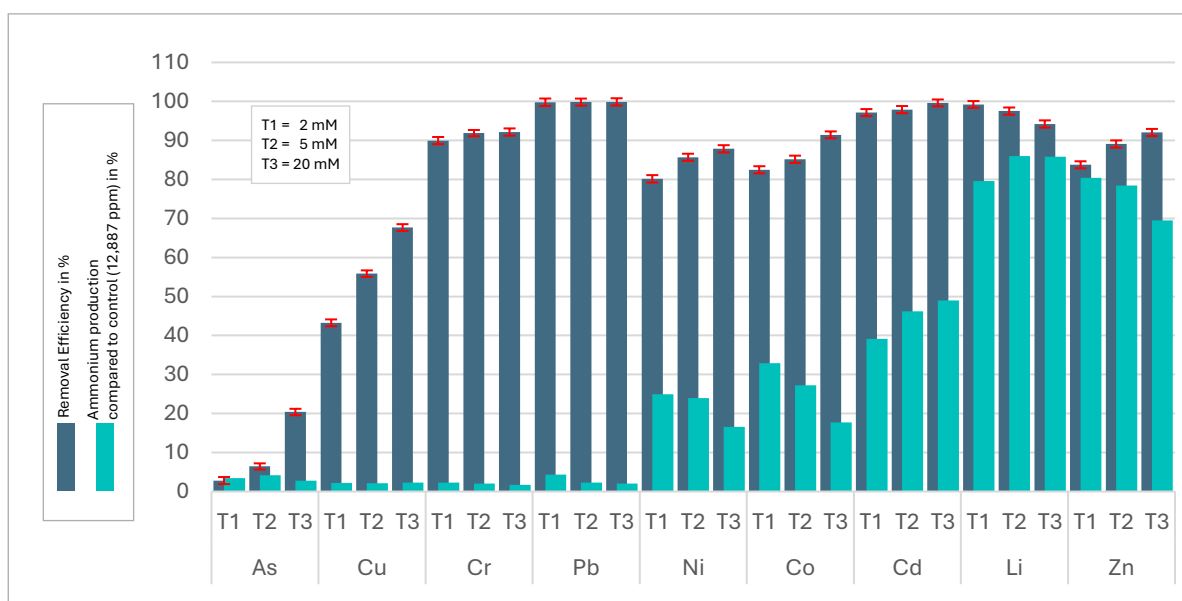


Figure 2. The figure presents removal efficiency (green bars) and ammonium production (purple bars) observed at the end of the EMMP experiment across different elements and three treatments (T1, T2, T3). The left Y-axis corresponds to both the removal efficiency, expressed as the average percentage of metal removal across five replicates (N = 5) and the ammonium production (single measurement N = 1), expressed as a percentage relative to the maximum value obtained in the control sample (12,877 ppm).

3.1.4. EMs removal efficiency

As observed in Figure 2, three groups can be identified based on removal efficiencies: low (2.82–20.39%), medium (43.25–67.66%), and high (80.16–99.88%). Removal efficiency trends were analysed based on increasing metal concentration from T1 to T3.

In the low range, arsenic exhibited efficiency increasing from 2.82% to 20.39% as metal concentration rose. In the medium range, copper also showed a steady improvement, increasing from 43.25% to 67.66% across treatments. The high removal efficiency range included seven metals. Lead exhibited the highest consistent removal rates, with an exceedingly small variation from 99.78% to 99.88%. In contrast, lithium experienced a slight decline, decreasing from 99.23% to 94.22%. The remaining metals in this category demonstrated progressive increases in removal efficiency: cadmium from 97.14% to 99.62%, chromium from 89.96% to 92.15%, nickel from 80.16% to 87.85%, cobalt from 82.48% to 91.44%, and zinc from 83.76% to 92.04%.

3.2. Micromorphological analysis of precipitates

3.2.1. Fraction > 1mm

Microscopic analysis of the precipitates performed using natural light microscopy for coarse fractions (>1 mm; Fig. 3) and scanning electron microscopy (SEM) for finer material (<1 mm; Figs. 4 and 5), revealed consistent features across treatments for most elements, with two dominant mineral phases typically present. However, arsenic samples deviated notably: only three isolated spheroids resembling carbonate phases were retained on the filter paper in T2, with material adhered to the paper filter and no evidence of widespread crystallisation. In copper treatments, the precipitates consisted primarily of fine, amorphous aggregates, and only sparse, poorly developed calcite crystals were observed in T1 and T2.

The first phase, predominantly calcitic, consisted of crystals exhibiting a variety of morphologies, including spherical, star-shaped, botryoidal, and other structural variations (Figure 3B, F, G, H, I and 5A to I). The second phase, phosphatic, was dominated by coffin-like and needle-like struvite crystals (Figure 3B, C, D, E and 5J to N). Within both fractions, these well-defined crystals were embedded in a fine powder aggregate (FPA) (<10 μm), primarily composed of calcite, which can be observed in Fig. 3A and 5A to N, and their detailed morphology in Fig. 5 O to R.

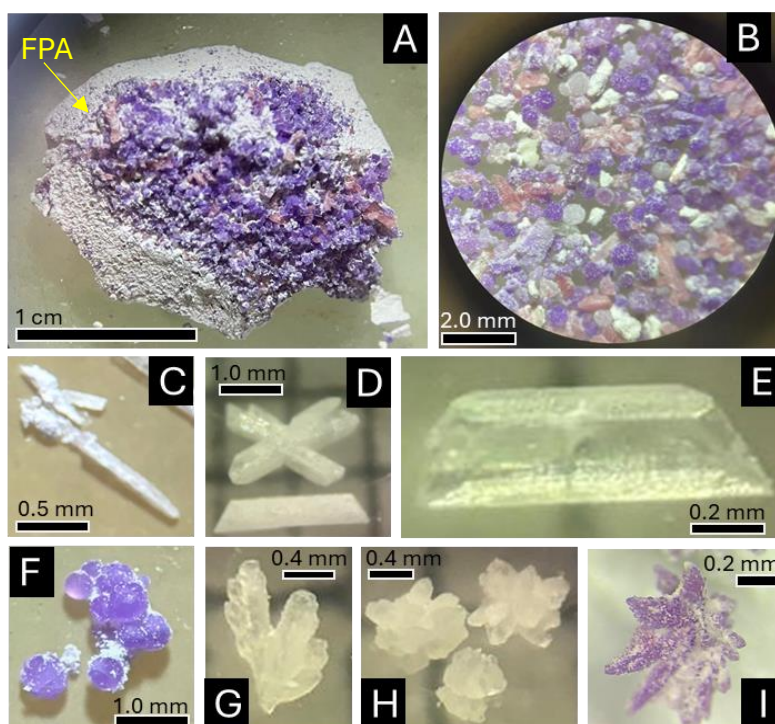


Figure 3. A) Co precipitate (T3) after oven drying step exhibiting larger crystals of calcite and struvite surrounded by a mass of very fine powder aggregate (FPA); B) Fraction of larger crystals under the microscope - natural light (Co-T3); C) Needle like crystal of calcite (Ni- T2); D) Butterfly and coffin-like struvite (Ni-T2); E) Coffin-like transparent struvite (Ni-T3); F) Spherical crystals are surrounded by a fine, loose calcitic powder (Co-T2); G, H) Star-like calcite (Cd-T2) and I) Star-like calcite (Co-T2).

3.2.2. Fraction < 1 mm

In this fraction the majority of treatments formed larger crystals of submillimetric calcite and struvite, consistently surrounded by a fine powder ($< 5\text{--}10\ \mu\text{m}$) composed predominantly of calcite (Figures 4-A to H and 5 A to R). Table 3 presents the sizes and predominant morphologies of calcite and struvite crystals across all treatments for all elements, as observed through scanning electron microscopy (SEM), highlighting the variability.

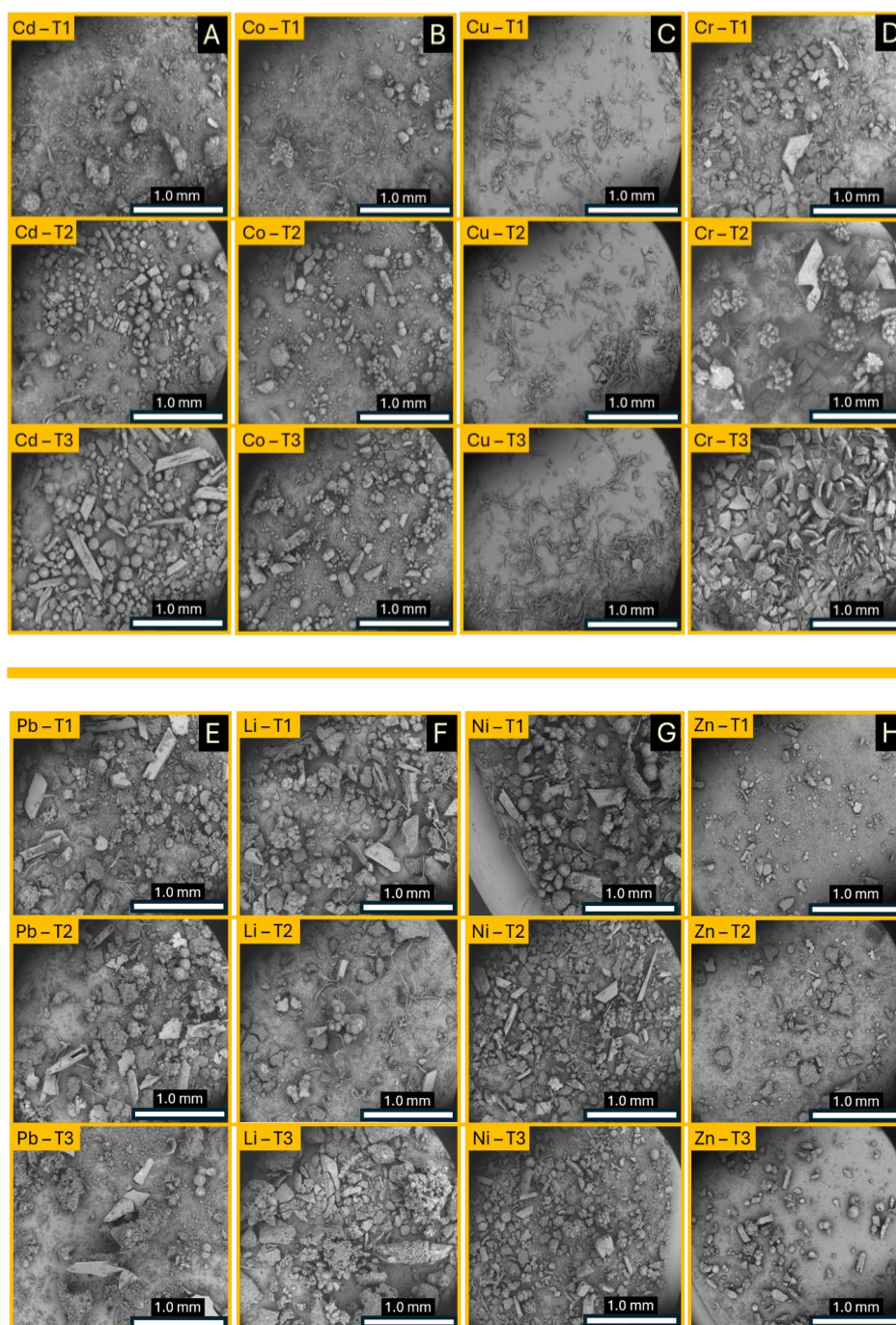


Figure 4. SEM backscattered images of a representative sample of precipitates formed in the presence of eight different metals under three treatments (T1, T2, T3). We used backscattered electron imaging as they enhanced resolution and contrast, allowing better differentiation of the morphological characteristics of the precipitates. Each column represents a metal (A: Cd, B: Co, C: Cu, D: Cr, E: Pb, F: Li, G: Ni, H: Zn), while each row corresponds to a treatment (top = T1, middle= T2 and bottom = T3). Arsenic was excluded as it did not yield enough material for analysis.

3.2.2.1. Micromorphology of calcite, struvite, and fine crystals aggregates

Arsenic was excluded from analysis due to insufficient mass, though a few spherical crystals (0.05–0.1 mm) resembling calcite were observed in T2. Copper primarily formed fine powder aggregates (Fig. 4C), with only a few sparse, small fibrous radial calcite crystals (0.05–0.10 mm) in T1 (Fig. 5F) and T2. Chromium produced calcite (0.20–0.65 mm) in T1 and T2, predominantly globular and star-shaped, whereas in T3 the observed fragments suggest that the material initially settled as a fine particulate layer, which later underwent mechanical or drying-induced cracking; this produced delaminated flakes that now appear as discrete shards under SEM observation (Fig. 4D; Fig. 5Q,R).

Across Li, Cd, Co and Ni treatments (Fig. 4 A, B, F and G), calcite crystal size progressively decreased from T1 to T3 despite the increase in precipitate mass. Lithium exhibited the broadest size range of crystals (0.10–0.65 mm), displaying spherical, globular, star-shaped, botryoidal (Fig. 5B), rare flower-like (Fig. 5E), and bone-like (Fig. 5I) morphologies, with fibrous forms and shards of aggregates of fine particulate layer appearing discretely in T2 and markedly in T3. Cadmium formed crystals (0.10–0.40 mm) with spherical (Fig. 5A), globular, star-shaped, and dumbbell-like (Fig. 5H) habits. Cobalt produced calcite crystals (0.01–0.40 mm), with donut (Fig. 5G) spherical, globular, and star-shaped (Fig. 5C,D) morphologies. Nickel formed predominantly spherical, globular, and star-shaped crystals (0.10–0.60 mm), with less variation in morphologies in T3.

Lead generated large crystals (0.10–0.60 mm), exhibiting predominantly spherical, globular, and star-shaped morphologies and larger crystals in T2. Zinc consistently formed small calcite crystals (0.05–0.30 mm), primarily spherical and globular, with the smallest crystals observed in T1.

Across all treatments, hollow coffin-like was the dominant struvite morphology (Fig. 5M). Arsenic and copper treatments did not form struvite crystals, while chromium generated coffin-like and prismatic struvite (0.10–0.85 mm) in T1 (Fig. 5L) and T2, but T3 contained only shards of fine powder aggregates (Fig. 5L).

Cadmium formed both coffin-like and prismatic crystals (0.20–0.90 mm) and cobalt exhibited only coffin-like crystals (0.05–0.40 mm), and for both elements the crystals size increased from T1 to T3. Lithium produced coffin-like and prismatic struvite (0.10–0.45 mm) in T1 and T2, decreasing in size from T1 to T3 whereas lead formed the larger coffin-like struvite crystals (0.20–1.0 mm) and for both metals the size of crystals decreased from T1 to T3. Nickel displayed diverse habits, including twinned, needle-like, and plate-shaped crystals (0.15–0.95 mm) (Fig. 5J, K, N), peaking in size at T2. Zinc consistently produced smaller struvite crystals (0.05–0.20 mm) across treatments.

The fine powder aggregate appears in all treatments as a fine powder to the naked eye and is predominantly characterised by spherical to coral-shaped morphologies, which are indicative of calcite as the principal mineral phase in this fraction (Fig 5 O-P). Fig. 5 Q-R displays submillimetre-scale plaques composed of aggregates of ultrafine particles, which are likely to include poorly crystalline and amorphous phases that can be found in lead T3, chromium T3, and lithium T3 samples, as well as across all copper treatments.

Table 3

Size and morphologies of calcite and struvite in the smaller fraction of the precipitates (< 1 mm). T = treatment, calcite morphologies = Sp (Spherical), G (Globular), St (Star-like), D (Dumbbell), F (Flower-like), Fr (Fibrous-radial), B (bone-like and struvite), C (Coffin-like), P (Prismatic) and N (Needle-like). N/A indicates no crystal was formed, only aggregated powder. The measured crystal sizes may vary across images due to natural heterogeneity in the powder samples, as individual selections from such materials rarely exhibit uniform dimensions.

Element	T	Calcite							Struvite				
		Morphologies							Size (mm)	Morphologies			Size (mm)
		Sp	G	St	D	F	Fr	B		C	P	N	
Cadmium	1	●	●	●	●				0.10-0.40	●	●		0.10-0.20
	2	●	●	●	●				0.10-0.30	●	●		0.20-0.30
	3	●	●			●			0.10-0.25	●	●		0.30-0.90
Cobalt	1	●	●	●				●	0.10-0.40	●			0.05-0.10
	2	●	●	●	●				0.10-0.30	●	●		0.10-0.25
	3	●	●	●					0.10-0.20	●			0.10-0.40
Chromium	1	●	●	●				●	0.20-0.40	●			0.10-0.60
	2	●	●						0.30-0.65	●			0.10-0.85
	3	-	-	-	-	-	-	-	N.A.	-	-	-	N/A
Lead	1	●	●	●					0.10-0.50	●			0.20-1.00
	2	●	●	●					0.20-0.60	●			0.20-0.70
	3	●	●	●					0.05-0.30	●			0.05-0.20
Lithium	1	●	●	●		●			0.10-0.65	●			0.10-0.45
	2	●	●						0.10-0.30	●	●		0.10-0.30
	3	●	●	●		●	●		0.10-0.15	●	●		0.10-0.20
Nickel	1	●	●	●	●		●		0.10-0.60	●			0.15-0.80
	2	●	●		●		●		0.10-0.30	●	●	●	0.20-0.95
	3	●	●	●					0.10-0.20	●			0.10-0.60
Zinc	1	●	●						0.10-0.20	●	●		0.05-0.10
	2	●	●						0.10-0.30	●			0.05-0.20
	3	●	●						0.05-0.20	●	●		0.10-0.30
Copper	1						●		0.05-0.10	-	-	-	N.A.
	2						●		0.05-0.10	-	-	-	N.A.
	3	-	-	-	-	-	-	-	N.A.	-	-	-	N.A.
Arsenic	1	-	-	-	-	-	-	-	N.A.	-	-	-	N.A.
	2	●							0.10-0.20	-	-	-	N.A.
	3	-	-	-	-	-	-	-	N.A.	-	-	-	N.A.

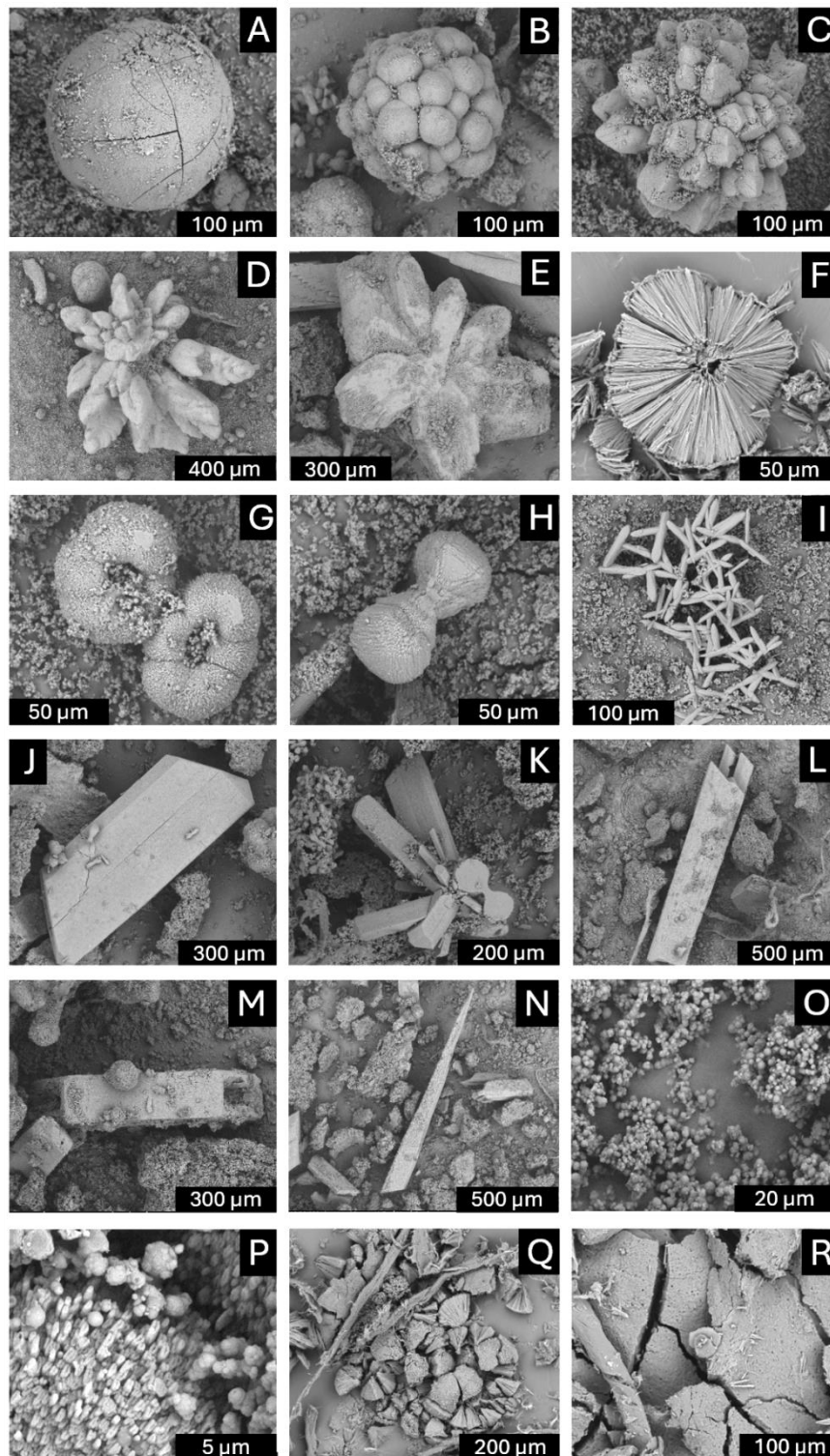


Figure 5. SEM micrographs of the predominant morphological variation of calcite and struvite crystals observed across various elements and treatment levels.). Backscattered electron imaging was used to enhance resolution and contrast. (A) Spherical calcite (Cd-T1); (B) Botryoidal calcite (Li-T1); (C,D) Star-shaped calcite (Co-T1 and T2); (E) Flower-shaped calcite (Li-T1); (F) Fibrous-radial calcite (Cu-T1); (G) Donut-shaped calcite (Co-T2); (H) Dumbbell calcite (Cd-T1); (I) Bone-like calcite (Li-T1); (J) Coffin-shaped struvite (Ni-T1); (K) Twinned struvite (Ni-T1); (L) Prismatic struvite (Cr-T1); (M) Detail of hollow struvite (Pb-T1); (N) Needle struvite (Ni-T1); (O) Morphology of fine powder aggregates (Co-T3); (P) Detail of fine powder aggregates showing coral-like microstructure (Co-T2); (Q) Mass aggregates in Cr-T3; (R) Detail of mass aggregate (Cr-T3).

3.3. Powder XRD

The diffractograms (Figure 6) show the precipitation patterns, indicating variations in the relative proportions of the two main crystalline phases, calcite and struvite, across treatments for each element. Minerals from the apatite group were also identified in some treatments through XRD Rietveld refinement. Although distinct apatite peaks were not visually discernible in the raw diffractograms, likely due to low abundance, peak overlap, and poor crystallinity, Rietveld refinement confirmed the presence of chlorapatite and hydroxyapatite, with contents ranging from 0.95% to 5.1%, depending on the EMs and treatment. Crystals of apatite were not observed in the larger fractions, suggesting that this phase is confined to the fine powder aggregate fraction. Arsenic and copper were excluded from the analysis due to insufficient mass for characterisation. Table 4 presents the relative percentages of the crystalline phases, calculated using Profex software version 5.4.1. These percentages are expressed as relative values, as no internal standard was employed to allow absolute quantification.

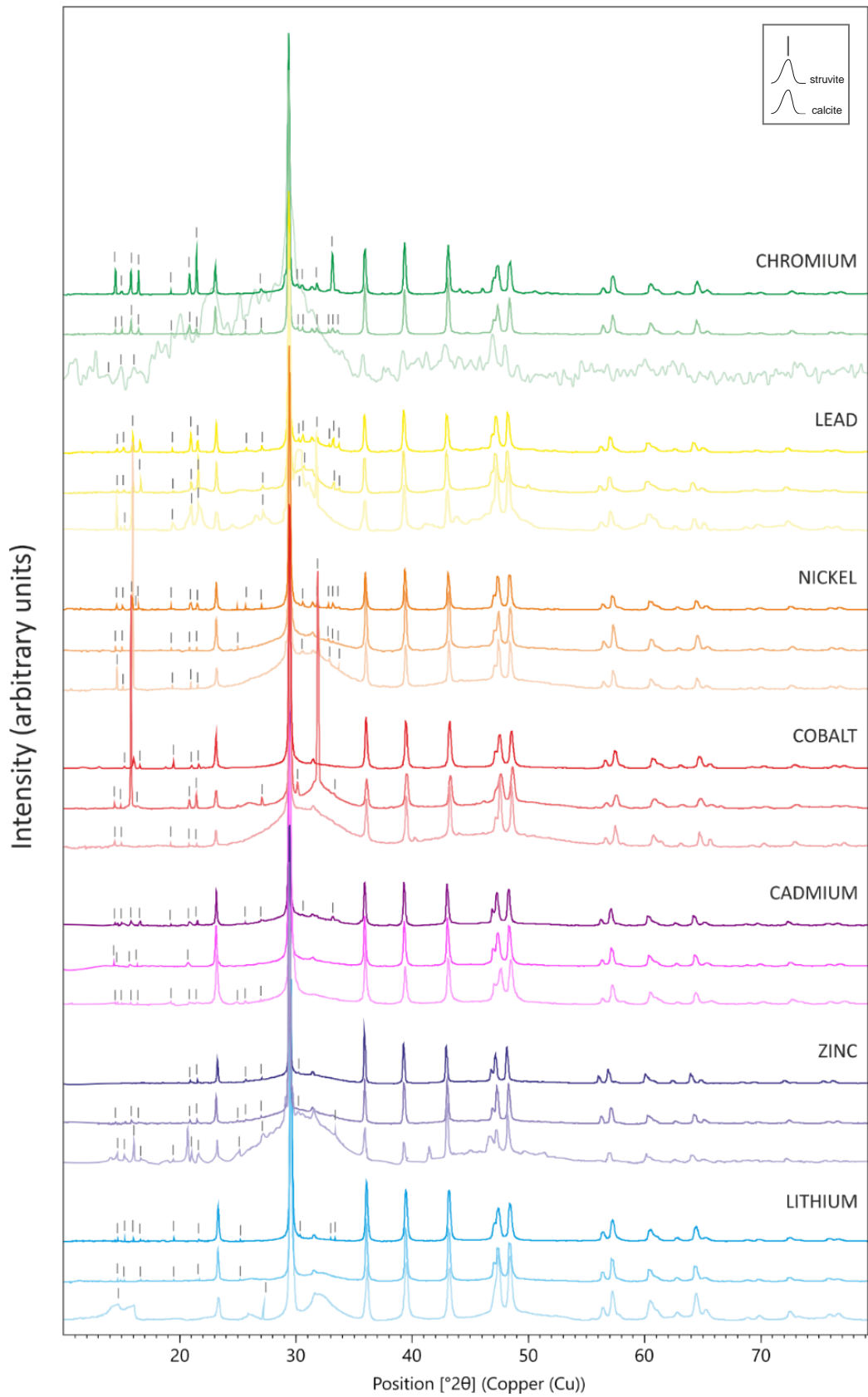


Figure 6. Stacked XRD diffractograms illustrating the crystallization of calcite and struvite in the presence of cobalt, nickel, lead, chromium, lithium, zinc, and cadmium across three treatment levels (T1 - top line, T2 - middle line, T3 - bottom line). The marked peaks correspond to struvite and the non-marked to calcite.

Table 4

Percentage of major (calcite and struvite) and accessory phases (apatite group) identified in the precipitates. Phase proportions were determined using Profex software based on relative abundances, without the application of an internal standard. T = Treatment; N.A. Non applicable. Trace (-) phase not identified.

Element	T	Main Phases		Minor and Accessory Phases			TOTAL (%)
		Calcite (%)	Struvite (%)	Chlor apatite (%)	Hydroxy apatite (%)	Apatite (%)	
Cadmium	1	87.15	9.32	-	4.37	-	99.84
	2	87.15	11.78	-	1.27	-	100.20
	3	96.36	3.78	-	-	-	100.14
Cobalt	1	91.66	6.03	2.44	-	-	100.13
	2	81.90	17.19	0.95	-	-	100.04
	3	91.47	8.61	-	-	-	100.08
Chromium	1	76.70	20.52	-	-	2.86	100.08
	2	89.84	9.07	-	-	1.25	100.16
	3	N.A.	N.A.	N.A.	N.A.	N.A.	N.A.
Lead	1	86.43	8.58	5.1	-	-	100.11
	2	82.84	12.87	4.4	-	-	100.11
	3	85.67	11.42	3.7	-	-	100.79
Lithium	1	87.04	8.81	3.11	-	-	99.95
	2	90.61	6.41	2.67	-	-	99.82
	3	N.A.	N.A.	N.A.	N.A.	N.A.	N.A.
Nickel	1	85.75	10.37	4.31	-	-	100.43
	2	92.24	5.85	2.04	-	-	100.13
	3	81.47	17.63	1.76	-	-	100.86
Zinc	1	95.42	4.60	-	-	-	100.02
	2	93.11	6.97	-	-	-	100.08
	3	90.88	9.24	-	-	-	100.12
Copper	1	N.A.	N.A.	N.A.	N.A.	N.A.	N.A.
	2	N.A.	N.A.	N.A.	N.A.	N.A.	N.A.
	3	N.A.	N.A.	N.A.	N.A.	N.A.	N.A.
Arsenic	1	N.A.	N.A.	N.A.	N.A.	N.A.	N.A.
	2	N.A.	N.A.	N.A.	N.A.	N.A.	N.A.
	3	N.A.	N.A.	N.A.	N.A.	N.A.	N.A.

The XRD diffractograms illustrate the evolving crystallisation behaviour of the two main phases in the system influenced by varying treatment levels across different elements. Chromium and lithium did not show enough crystallinity in T3 for a precise calculation of main phase percentages. For nickel, lead, chromium, lithium, and cadmium, sharper and more intense peaks are observed at T1, which progressively diminish toward T3. This trend suggests a higher degree of crystallinity at treatment levels with lower concentration of EMs. Interestingly, cobalt and zinc deviate from this pattern, displaying more intense and sharper peaks at T2 compared to T1, indicating that intermediate treatment levels create conditions more favourable for crystallisation, which then decline at T3. Arsenic and copper did not yield sufficient precipitate for XRD analysis.

The relative proportions of calcite and struvite varied across elements and treatments, with calcite consistently dominating the precipitates. Cobalt and lead displayed similar trends, with calcite reaching its highest proportions in T1 (91.66% and 86.43%, respectively), decreasing at T2 (81.90% and 82.84%), and increasing again at T3 (91.47% and 85.67%). Struvite showed an inverse pattern, peaking in T2 for both elements (17.19% for cobalt and 12.87% for lead) with lower levels in T1 and T3.

Cadmium and nickel also exhibited high calcite content across all treatments. Calcite content for cadmium was lowest at T2 (87.15%) and peaked at T3 (96.36%), while nickel displayed the highest calcite proportion at T2 (92.24%) and the lowest at T3 (81.47%). Struvite proportions followed complementary trends, with cadmium reaching its highest struvite content at T2 (11.78%) and nickel at T3 (17.63%).

Chromium, lithium, and zinc showed calcite as the predominant phase, with varying degrees of struvite content. Chromium exhibited calcite proportions of 76.7% at T1 and 89.8% at T2, while struvite decreased from 20.52% to 9.07%; no data were available for T3 due to insufficient precipitate mass. Lithium treatments showed calcite proportions of 87.04% at T1 and 90.61% at T2, with struvite proportions at 8.81% and 6.41%, respectively. Zinc showed decreasing calcite content from T1 to T3 (95.42% to 90.88%), while struvite proportions increased steadily, peaking at 9.24% in T3. Data for copper is unavailable due to insufficient precipitate mass for characterisation.

In addition to calcite and struvite, minerals from the apatite group were identified in cadmium, lead, lithium, chromium and nickel treatments. The highest proportions were found in lead (5.11% in T1 and 4.40% in T2), followed by nickel (4.31% in T1 and 2.04% in T2), lithium (3.11% in T1 and 2.67% in T2), cadmium (4.37% in T1 and 1.27% in T2), chromium (2.86% in T1 and 1.25% in T2) and cobalt (2.44% in T1 and 0.95% in T2). No apatite-group phases were detected in zinc treatments.

4. Discussion

Our study reveals that metal immobilisation in EMMP emerges from the interplay of multiple, co-occurring mechanisms, challenging the conventional assumption that mineralisation is driven exclusively by ureolytic carbonate precipitation in ureolytic systems that rely on crude urease extracts. While urease-mediated urea hydrolysis remains a key pathway—governing pH shifts and carbonate availability—our results demonstrate that mineral formation, phase-specific crystallisation dynamics and retention efficiency are additionally shaped by secondary processes [8][63][64].

Despite the well-established pH optimum for urease activity in alkaline environments, we observed sustained carbonate formation under mildly acidic conditions (pH ~5), particularly in Cr treatments. These results align with previous reports of residual urease activity at low pH values [65][66], possibly preserved through structural stabilisation by biomolecules present in crude soybean extract or bone meal [66][67]. The presence of proteins and polysaccharides may shield catalytic sites via hydration shells or interact with mineral surfaces to buffer local pH fluctuations, maintaining enzymatic function within microenvironments [68].

Crucially, metal retention did not consistently correlate with precipitate mass. Several elements, including Cr, Ni, and Pb, showed increasing immobilisation despite declining mineral yield, indicating that non-crystalline or surface-bound forms played a substantive role. This decoupling suggests that biosorption and mineral surface interactions can become dominant under high-metal conditions. Prior work has shown that the sorption capacity of soybean-derived biosorbents increases with metal ion concentration, driven by stronger concentration gradients and the accessibility of functional groups on organic or mineral surfaces [69].

Collectively, these findings support a revised model of EMMP function in which carbonate and phosphate precipitation operate alongside—and are potentially enhanced by—biosorption and surface complexation mechanisms. These coexisting pathways are not mutually exclusive but act synergistically across varying pH and concentration regimes, contributing to the robust immobilisation performance observed across treatments.

To evaluate the relative contribution of these mechanisms, we classified the studied elements based on their removal efficiency (low, medium, and high). We analysed their behaviour in relation to system pH, precipitate composition, enzymatic performance, and inferred mineral–biomolecule interactions.

4.1. Metals with low immobilisation efficiency

Arsenic consistently exhibited the lowest removal efficiency across all treatments, with minimal solid-phase recovery, minor ammonia release, and a persistently acidic final pH. Only a few carbonate-like spheroids were detected in treatment group T2, and no recoverable mass was obtained, as the material remained firmly adhered to the filter medium, consistent with an amorphous or colloidal composition. These findings point to a fundamental incompatibility of As(III) with both mineral and biomolecular retention mechanisms under the experimental conditions.

Limited carbonate mineral formation is likely attributable to both the chemical neutrality of As(OH)₃ and its inhibitory effect on urease activity. Trivalent arsenic, the dominant aqueous species at pH < 9, does not favour electrostatic interaction with carbonate anions and does not substitute into calcite or aragonite lattices [70][71]. Simultaneously, As(III) binds to thiol groups at the urease active site, disrupting the coordination environment essential for catalysis [72]. While specific kinetic data for urease inhibition by arsenite remain limited, thermodynamic studies demonstrate that As(III) forms stable, enthalpically favoured complexes with thiol-containing ligands, supporting a plausible mechanism of enzyme inhibition via covalent modification of active-site cysteines [73]. This contrasts with the non-competitive inhibition observed for divalent metals such as Cd²⁺ and Co²⁺. While arsenic is not typically classified among the most potent urease inhibitors [74], the more elevated concentrations used here (2–20 mM) and the system's acidic conditions likely exacerbated its inhibitory impact. As carbonate production depends directly on urea hydrolysis, the resulting suppression in alkalinity and carbonate supersaturation effectively precluded nucleation of classical polymorphs.

Direct phosphate-based pathways also failed to stabilise arsenic. Unlike cationic metals such as Pb²⁺ or Cr³⁺, which form stable phosphate precipitates or integrate into apatite analogues, As(III) does not engage in such reactions under acidic and circumneutral pH. Arsenate (AsO₄³⁻)

can substitute isomorphically for phosphate in hydroxyapatite [75], but arsenite lacks the necessary tetrahedral geometry and formal charge. Prior studies confirm that $\text{As}(\text{OH})_3$ interacts weakly with phosphate ligands and fails to form discrete mineral phases without prior oxidation [76]. Competitive interactions between arsenite and phosphate may also further inhibit retention on reactive surfaces in acidic settings [77]. These observations are consistent with the absence of visually or analytically detectable As-phosphate precipitates in this system.

Alternative immobilisation routes via biomolecular association were likewise ineffective. Arsenite, being uncharged, exhibits limited electrostatic affinity for anionic groups such as carboxylates or phosphates. Instead, it forms covalent bonds with thiol groups, preferentially coordinating with two or more spatially proximate cysteine residues to yield tridentate complexes [78]. Such coordination environments are characteristic of metallothioneins and phytochelatins but are not prevalent in crude soybean extracts. Even where low-affinity binding to thiols might occur, the entropically constrained nature of such interactions in disordered systems limits the formation of persistent complexes [79]. Arsenite's limited coordination versatility further precludes its participation in the polyvalent interactions required for stable colloidal or precipitated complexes. As a result, arsenic may have remained predominantly in the aqueous phase, consistent with both the solution chemistry of $\text{As}(\text{OH})_3$ and the absence of solid-phase retention across all tested pathways.

4.2. Metals with medium immobilisation efficiency

Copper exhibited moderate removal efficiency despite persistently low pH, minimal ammonium generation, and variable mass recovery. No well-formed struvite or calcite crystals were recovered, as only fine mass aggregate was formed with sparse radial carbonate-like morphologies visible in SEM images of T1 and T2. These results indicate suppression of carbonate mineralisation pathways, consistent with inhibition of ureolysis.

This is consistent with copper's known role as a potent, time-dependent inhibitor of urease. Cu^{2+} binds rapidly to cysteine residues near the nickel-active site, forming an initial enzyme-inhibitor complex that undergoes slow rearrangement into a tightly bound inhibitory state. The resulting inhibition follows a biphasic, slow-binding mechanism [72], with equilibrium inhibition constants in the nanomolar range, second only to Hg^{2+} in potency. Urease inhibition by Cu^{2+} is driven by its high affinity for thiol-containing residues, notably cysteines near the active site. Even in the absence of free sulphur species, Cu^{2+} forms stable complexes that disrupt catalysis and suppress carbonate production. Spectroscopic data confirm partial thiol coordination, with additional binding to histidine and carboxylate residues contributing to the loss of activity [80]. As a consequence, the alkaline conditions required for nucleation of calcium carbonate polymorphs were never attained.

In the phosphate-bearing systems, however, direct Cu-phosphate interactions could occur, even in the absence of significant carbonate nucleation. Madsen's kinetics study [81] on copper phosphate crystallisation from acid solutions identified three phases— CuNH_4PO_4 , $\text{CuHPO}_4 \cdot \text{H}_2\text{O}$, and Cu_2OHPO_4 —out of which only Cu_2OHPO_4 formed well-defined crystals; the rest appeared as poorly crystalline spherulites that could not be readily separated or distinguished microscopically. This observation underlines that copper phosphate precipitates tend toward

amorphous or colloidal forms, which may pass through filters or remain intimately bound to organic matter rather than forming discrete mineral deposits in our system.

Moreover, copper hydroxide ($\text{Cu}(\text{OH})_2$), well-known to be metastable in aqueous conditions, readily transforms into CuO via dissolution–reprecipitation mechanisms involving the $\text{Cu}(\text{OH})_4^{2-}$ complex [82]. In systems containing bone meal and organic polymers, transient $\text{Cu}(\text{OH})_2$ may form and then locally convert to poorly crystalline CuO rather than persist as ordered hydroxide minerals. This pathway suggests the possible formation of nanoparticulate oxide phases, even under mild pH conditions, through non-classical pathways.

Taken together, these findings support a model in which copper immobilisation in the current context occurred predominantly through adsorption onto amorphous Cu-phosphate or Cu-oxide nanoparticles or through association with organic–mineral complexes. Such phases, whether precipitated or sorbed, would likely remain in the form of fine aggregate mass and contribute to medium-range copper sequestration without producing crystallographically identifiable minerals.

4.3. Metals with high immobilisation efficiency

Chromium consistently produced an acidic environment, with pH decreasing across treatments. This trend, coupled with low ammonium and precipitate mass production, suggests significant ureolytic inhibition, particularly at higher Cr concentrations. Previous studies have shown that Cr^{3+} can inhibit urease activity by binding to key functional groups within or near the enzyme's active site or by interfering with Ni^{2+} coordination essential for catalysis [83]. Despite this, Cr removal remained high across treatments, indicating that the contribution of non-ureolytic pathways to its immobilisation played a significant role.

Crystallisation patterns support this interpretation. While T1 and T2 featured the formation of calcite and struvite, with crystal morphologies ranging from globular to coffin-like, no identifiable crystals were recovered in T3. This absence of crystalline phases in T3, coupled with sustained high removal, suggests that Cr is predominantly retained in amorphous or nanocrystalline forms. The detection of minor apatite fractions in T1 and T2 suggests phosphate interactions may contribute to retention under moderately acidic conditions. However, substitution of Cr^{3+} into carbonate or phosphate crystal lattices is considered unlikely due to its smaller ionic radius and higher charge density relative to Ca^{2+} [84]. Instead, surface complexation, especially onto amorphous carbonate or phosphate-rich domains, is a more plausible mechanism [85][86].

At higher concentrations, the predominant retention mechanism likely involved precipitation of $\text{Cr}(\text{OH})_3$ or adsorption onto interstitial and organic surfaces. XAFS studies confirm that Cr^{3+} is typically associated with non-crystalline domains or exists as surface-bound hydroxide precipitates under similar conditions [87][88]. Interactions with functional groups such as carboxyl ($-\text{COO}^-$), hydroxyl ($-\text{OH}$), and phosphate ($-\text{PO}_4^{3-}$) may further stabilise Cr in situ.

In contrast, Pb^{2+} behaved in a manner consistent with dominant mineralisation pathways. pH values remained stably alkaline across all treatments, and removal efficiency exceeded 99.78%. Ammonium production was low, yet crystalline phases formed consistently. Unlike Cr^{3+} , Pb^{2+} does not appear to inhibit urease strongly under the tested conditions, possibly due to

sequestration by organic ligands that limit direct enzyme interaction [89]. Furthermore, reduced ammonium levels may result not from inhibited ureolysis but rather from NH_4^+ incorporation into minerals such as struvite or association/adsorption with/into mineral phases and secondarily, with biomolecules.

Mineralogical analysis revealed stable crystallisation of calcite and phosphate phases in Pb treatments. Chlorapatite was detected at 5.10% in T1, 4.40% in T2, and 3.70% in T3, suggesting persistent Pb-phosphate precipitation. Struvite content also increased over treatments, indicating sustained phosphate-driven immobilisation. Pb^{2+} may be incorporated into carbonate phases via coprecipitation or occlusion rather than direct lattice substitution owing to its ionic radius and low solubility product under alkaline conditions [90].

Additionally, interactions with organic matrices likely stabilised Pb through surface complexation and ion exchange. Functional groups, such as carboxylates and amines, in bone meal and soy derivatives have been documented to have an affinity for Pb binding [69]. These biomolecules may also influence crystal morphology, promoting nucleation or stabilising amorphous intermediates.

Together, the comparison highlights a mechanistic dichotomy: while Cr^{3+} relies more heavily on adsorption and hydroxide precipitation under acidic, low-ureolysis conditions, Pb^{2+} is efficiently retained via robust, high-pH mineralisation routes, supported by both carbonate and phosphate phases. The roles of organic matter in both systems remain secondary but may contribute to enhanced stability through molecular interactions and matrix entrapment.

Nickel (Ni), cobalt (Co), cadmium (Cd), lithium (Li), and zinc (Zn) formed a coherent group within the alkaline pH domain, exhibiting converging behaviours concerning ureolytic activity, precipitation patterns, and removal efficiency. All five elements maintained pH values above 7.5 across treatments, enabling carbonate and phosphate mineralisation pathways to operate more effectively than in acidic systems.

In terms of ammonium production, Ni and Co exhibited intermediate levels indicative of moderate inhibition of urease activity. Cd, Li, and Zn reached significantly higher ammonium concentrations, suggesting a more active ureolytic environment conducive to mineral precipitation. These values, in combination with consistently high pH, contributed to stable precipitation of crystalline phases, as supported by SEM and PXRD data.

Nickel and cobalt each formed crystalline phases comprising both struvite and calcite, with minor fractions of chlorapatite suggesting limited phosphate-based retention. Their removal efficiencies increased steadily from T1 to T3, reaching 87.85% for Ni and 91.44% for Co. Moreover, both metals exhibited similar parametric profiles across treatments, including pH, ammonium release, and precipitation behaviour. However, their chemical behaviour during immobilisation likely diverged. The co-occurrence of carbonate and phosphate minerals supports a mixed-mode mechanism involving coprecipitation or surface association with multiple solid phases. Ni^{2+} was likely retained through adsorption onto calcite, with limited structural incorporation [91], and may have formed Ni-struvite ($\text{NH}_4\text{NiPO}_4 \cdot 6\text{H}_2\text{O}$) via rapid crystallisation from transient amorphous precursors. Co^{2+} , in contrast, appears to disrupt calcite nucleation [92] and may have followed a slower, two-step crystallisation pathway involving more persistent colloidal intermediates, ultimately yielding Co-struvite or cobalt phosphate phases [93]. The apparent instability of Co-struvite, which tends to transform into Co-dittmarite upon air exposure,

further supports this divergence. These findings suggest that, despite exhibiting comparable parametric trends, Ni and Co underwent immobilisation through distinct crystallisation pathways shaped by differences in precipitation kinetics and coordination chemistry. It is therefore likely that most immobilisation occurred through partial substitution of Ni²⁺ and Co²⁺ into Ca- and Mg-bearing mineral lattices and through adsorption onto mineral surfaces rather than through direct association with biomolecular components of the system.

Cadmium demonstrated particularly high ammonium production and extensive mineral crystallisation. PXRD patterns revealed dominant calcite and moderate struvite phases, alongside minor hydroxyapatite detected in T1 and T2. The increase in removal efficiency from 97.14% to 99.62% indicates highly effective immobilisation, likely driven by simultaneous carbonate and phosphate precipitation pathways. These findings align with previous studies reporting that Cd²⁺ can substitute for Ca²⁺ in calcite, forming the isostructural otavite (CdCO₃) via chemisorption or lattice integration [95][96][97]. Kinetic studies further suggest that such substitution proceeds rapidly on porous calcite, where heteroepitaxial growth of otavite occurs at crystallographic interfaces, particularly under neutral pH conditions [107]. While phosphate incorporation is also feasible, the dominant mechanism in this system likely involved direct reaction with carbonate surfaces and internal pore domains, rather than complexation with organic matter.

Lithium, although less commonly studied in these systems, exhibited consistently high ureolytic activity, as evidenced by stable alkaline pH and ammonium production rates exceeding 79% across treatments. Its negligible interaction with urease cofactors such as Ni²⁺ ensures minimal inhibition and uninterrupted urea hydrolysis [98]. Crystalline precipitates included predominantly calcite (87.04–90.61%), minor struvite (6.41–8.81%), and accessory chlorapatite (~3%), reflecting carbonate-dominated mineralisation. Lithium removal efficiency remained above 94%, peaking at 99.23% in T1, but declined progressively with increasing Li⁺ concentrations. This trend is consistent with its small ionic radius, monovalent charge, and high hydration energy, which limit lattice incorporation into both carbonate and phosphate minerals [99][100]. At higher concentrations, Li⁺ interferes with crystal growth by inhibiting step-edge attachment, promoting rapid nucleation and fibrous morphologies while reducing long-range order, as reflected by narrowing crystal size distributions and decreased crystallinity in T3. These observations indicate that lithium retention is closely linked to incorporation within well-formed crystalline carbonate phases. As crystallinity decreases, removal efficiency declines, suggesting that amorphous or nanocrystalline domains provide limited retention capacity since the mass precipitation did not decrease substantially from T1 to T3, only the level of crystallinity. Lithium's weak affinity for phosphate groups further limits its role in struvite or chlorapatite formation, and its contribution to phosphate mineralisation appears negligible [101][102].

Zinc removal was consistently high across all treatments, potentially favoured by the alkaline pH and sustained ureolytic activity. Although no Zn-specific crystalline phases were detected, retention may have occurred via partial substitution into calcite or adsorption onto mineral surfaces. Ghizellaoui and Euvrard [108] demonstrated that Zn²⁺ inhibits the growth of calcite crystals and alters their morphology, likely through surface adsorption and coprecipitation with CaCO₃, forming Ca–Zn carbonates at higher concentrations. These effects may account for the observed crystallisation patterns and progressive Zn removal. In parallel, the presence of struvite in the system suggests that Zn²⁺ may also interact with phosphate ligands.

Rouff and Juarez [109] reported that Zn^{2+} binds to struvite surfaces via inner-sphere complexation and, under increased Zn concentrations, may promote the formation of poorly crystalline Zn–phosphate or hydroxide precipitates. Taken together, these studies suggest that Zn immobilisation in the present system likely involved a combination of sorption and co-precipitation processes associated with both carbonate and phosphate phases.

Collectively, these five elements (Ni, Co, Cd, Li, and Zn) displayed converging mechanistic traits characterised by compatibility with ureolytic activity, consistently alkaline pH, and the formation of crystalline carbonate and phosphate phases. Low-moderate to high ammonium production in these systems suggests that enzymatic activity remained sufficiently active to support carbonate mineralisation, while the presence of struvite and apatite indicates that phosphate-mediated metal immobilisation may have also occurred. Among them, cadmium, lithium, and zinc exhibited higher ammonium levels, suggesting enhanced compatibility with the urease-mediated precipitation pathway. Conversely, nickel and cobalt produced lower ammonium levels and a greater proportion of calcite, consistent with a mixed-mode pathway involving both ureolytic and non-ureolytic mineralisation routes.

Ammonium retention in these systems was likely governed by a combination of ureolysis-driven release and subsequent incorporation into mineral phases or association with organic matrices. Under phosphate-rich conditions, ammonium was structurally integrated into struvite ($\text{NH}_4\text{MgPO}_4 \cdot 6\text{H}_2\text{O}$), as demonstrated in urease-based systems by Gowthaman et al. [23] and in *Azotobacter* cultures by Rivadeneira et al. [111]. In carbonate-dominated environments, ammonium may have been transiently retained within amorphous calcium carbonate (ACC) or occluded during rapid crystal growth. Farghali et al. [24] noted that ammonium can interact with both mineral and organic components under alkaline conditions, contributing to its sequestration. Experimental evidence by Söhnle et al. [112] further supports this view, showing that while NH_4^+ does not alter the crystallisation mechanism of calcite, it significantly inhibits crystal growth rates, implying a kinetic rather than structural role in ammonium–carbonate interactions. Together, these studies suggest that ammonium retention likely occurs via multiple, phase-dependent pathways, modulated by both chemical environment and crystallisation kinetics. Organic amendments such as soybean derivatives and bone meal may have further stabilised ammonium via weak complexation with protein-bound carboxylate or phosphate groups. This is consistent with findings that organic matter—particularly humic acids—can enhance ammonium retention through interactions with surface functional groups such as hydroxyl and carboxyl moieties [113]. These concurrent pathways may explain the observed balance between ammonium production and retention, with high-pH systems maintaining sufficient free NH_4^+ to support precipitation while limiting its loss.

Beyond mineral precipitation, organic matrices such as soybean derivatives and bone meal likely contributed to immobilisation via complexation with functional groups, including carboxylates, amines, and thiols. Cobalt and nickel are known to coordinate with histidine and cysteine residues in metalloproteins [114], while cadmium displays a high affinity for thiol-rich peptides such as phytochelatins and metallothioneins [93]. Lithium and zinc, although less reactive toward sulphur donors, can engage with phosphate and carboxylate ligands, particularly in hydrated or amorphous matrices [69]. These biomolecular interactions likely stabilised transient or poorly crystalline mineral phases and enhanced retention under conditions where

precipitation kinetics were limited. However, while biomolecular associations are plausible, they remain speculative under the tested conditions and require further studies for validation.

The persistence of high pH in all systems, minimal evidence of enzyme inhibition, and the repeated detection of calcite and struvite in PXRD profiles further support this interpretation. Taken together, these results highlight the robustness of ureolytic and phosphate-driven pathways in facilitating efficient immobilisation of transition and post-transition metals under alkaline conditions.

5. Conclusions

This study demonstrated that Enzyme-Mediated Multiphase Precipitation (EMMP) is an effective metal immobilization strategy, achieving high removal efficiencies for most tested EMs. Removal rates exceeded 95% for lead, cadmium, and zinc and 80% for cobalt, nickel, and lithium, while chromium also exhibited high removal efficiency (exceeding 90%) despite notable urease inhibition, whereas copper showed intermediate and arsenic exhibited lower removal efficiencies, likely due to their inhibitory effects on enzymatic and precipitation pathways. The relative immobilization efficiency followed the sequence: Pb > Cd > Li > Cr > Zn > Co > Ni > Cu > As, underscoring the differential responses of metals within the EMMP system.

The primary immobilization pathway was governed by the ureolytic process, wherein urease catalyses urea hydrolysis, generating ammonium and carbonate. This reaction promoted the formation of calcite and struvite, enabling both direct precipitation of metal carbonates and co-precipitation within evolving mineral phases. However, secondary mechanisms—including ion exchange, surface adsorption, and biomolecule-mediated interactions—further enhanced metal retention by stabilizing intermediates and expanding the range of immobilization pathways beyond carbonate mineralization. Notably, for several metals including Cr, Ni, and Pb, immobilisation increased even where precipitate mass declined, suggesting the significant contribution of biosorption, surface complexation, and non-crystalline retention pathways under metal-rich conditions. Direct phosphate precipitation also played a key role in immobilising certain metals, particularly lead, where phosphate precursors influenced the crystallogenesis of both calcite and struvite phases. These findings highlight that EMMP operates through a combination of enzymatic and non-enzymatic pathways, enhancing its versatility under varied geochemical constraints.

Additionally, ammonium mitigation was achieved through multiple parallel mechanisms, including incorporation into mineral structures such as struvite and metal-substituted struvite, adsorption onto mineral surfaces, and chelation with biomolecules in the crude urease extract. Compared to the control, which was set at 100%, ammonium production was highest for lithium and zinc, exceeding 78%, moderate for cadmium, nickel, and cobalt (16.56–48.97%), and lowest for chromium, copper, lead, and arsenic (below 5%), reflecting differential impacts on urease activity. Importantly, EMMP proved effective even under mildly acidic conditions (pH ~5.0), traditionally considered suboptimal for urea hydrolysis, suggesting that the crude extract retains partial catalytic activity in less favourable environments. These results confirm that EMMP can simultaneously immobilize metals and regulate ammonium dynamics, enhancing its value as a multifunctional remediation tool.

While this study examined a wide array of EMs, it primarily focused on their individual behaviours rather than their interactions within complex multi-metal systems. However, real-world contaminated environments typically contain mixtures of metals that can influence each other's precipitation and immobilization dynamics. For example, the strong urease inhibition caused by arsenic observed in this study may significantly impact EMMP performance in mixed-metal scenarios. Future research should investigate metal-metal interactions within EMMP systems to determine whether competitive inhibition, synergistic effects, or preferential precipitation pathways emerge in multi-contaminant settings. Understanding these interactions will be essential for optimizing EMMP performance in real-world applications and ensuring its reliability as a remediation strategy. In particular, the linearly increasing removal trend observed for copper across treatments, as discussed in Section 4.2, may reflect unique, non-mineralisation-dominated pathways and should be explored further in future studies.

Additionally, while this study investigated EMMP in aqueous systems, its effectiveness in soil environments remains to be fully explored. The presence of soil minerals, organic matter, and varying geochemical conditions could influence precipitation pathways, metal immobilization efficiency, and long-term stability. Future research should focus on applying EMMP to contaminated soils, assessing its interactions with soil matrices, and evaluating potential limitations or enhancements that arise from soil heterogeneity, porosity, and microbial activity. These insights will be critical for translating EMMP from controlled laboratory conditions to large-scale field applications.

Beyond its remediation potential, EMMP aligns with circular economy principles and the GHG Protocol [115] by utilizing food waste-derived enzymes and mineral waste sources. It offers a low-energy, sustainable alternative to conventional chemical precipitation methods. Its ability to enhance metal sequestration while minimizing greenhouse gas emissions supports broader environmental applications, including contaminated soil stabilization and wastewater treatment.

To enhance the applicability of EMMP, future research should focus on three key aspects: improving mechanistic understanding by identifying the specific enzymes and biochemical interactions responsible for secondary immobilization pathways; assessing the long-term stability of immobilized metals under variable environmental conditions, including pH fluctuations, redox changes, and biological activity; and validating large-scale applications through field trials to refine process parameters and assess feasibility in diverse contamination scenarios. Additionally, it is essential to evaluate potential by-products of the process, particularly the concentrations of calcium, magnesium, iron, manganese, bromate, chlorine, and other compounds in treated water, to ensure compliance with water quality standards and mitigate unintended environmental impacts.

Overall, this study underscores the versatility of EMMP as an innovative, multifunctional biotechnological approach for heavy metal immobilization and ammonium mitigation, with strong potential for scalable environmental applications.

References

[1] IPCC, 2022: *Climate Change 2022: Impacts, Adaptation, and Vulnerability*. Contribution of Working Group II to the Sixth Assessment Report of the Intergovernmental Panel on Climate Change [H.-O. Pörtner, D.C. Roberts, M. Tignor, E.S. Poloczanska, K. Mintenbeck, A. Alegría, M. Craig,

S. Langsdorf, S. Löschke, V. Möller, A. Okem, B. Rama (eds.]). Cambridge University Press. Cambridge University Press, Cambridge, UK and New York, NY, USA, 3056 pp., doi:[10.1017/9781009325844](https://doi.org/10.1017/9781009325844).

[2] FAO. 2021. The State of the World's Land and Water Resources for Food and Agriculture – Systems at breaking point. Synthesis report. Rome.

[3] Li, W., Zhang, Y., & Achal, V. (2022). Mechanisms of cadmium retention on enzyme-induced carbonate precipitation (EICP) of Ca/Mg: Nucleation, chemisorption, and co-precipitation. *Journal of Environmental Chemical Engineering*, 10(3), 107507. <https://doi.org/10.1016/j.jece.2022.107507>

[4] Bian, Y., Chen, Y., Zhan, L., Ke, H., Gao, Y., Wang, Q., & Qi, G. (2024). An Enzyme-Induced Carbonate Precipitation Method for Zn²⁺, Ni²⁺, and Cr(VI) Remediation: An Experimental and Simulation Study. *Applied Sciences*, 14(15), 6559. <https://doi.org/10.3390/app14156559>

[5] Xu, W., Zheng, J., Cui, M., & Lai, H. (2025). Enzyme-Induced Carbonate Precipitation for the Stabilization of Heavy Metal-Contaminated Landfill Soils: A Sustainable Approach to Resource Recovery and Environmental Remediation. *Sustainability*, 17(10), 4630. <https://doi.org/10.3390/su17104630>

[6] Wilcox, S. M., Mulligan, C. N., & Neculita, C. M. (2025). Mineral Carbonation for Carbon Sequestration: A Case for MCP and MICP. *International Journal of Molecular Sciences*, 26(5), 2230. <https://doi.org/10.3390/ijms26052230>

[7] Mallick, S., Pradhan, T., & Das, S. (2025). Bacterial biomineralization of heavy metals and its influencing factors for metal bioremediation. *Journal of Environmental Management*, 373, 123977. <https://doi.org/10.1016/j.jenvman.2024.123977>

[8] Ahenkorah, I., Rahman, M. M., Karim, M. R., Beecham, S., & Saint, C. (2021). A Review of Enzyme Induced Carbonate Precipitation (EICP): The Role of Enzyme Kinetics. *Sustainable Chemistry*, 2(1), 92-114. <https://doi.org/10.3390/suschem2010007>.

[9] Whiffin, V. S., van Paassen, L. A., & Harkes, M. P. (2007). Microbial Carbonate Precipitation as a Soil Improvement Technique. *Geomicrobiology Journal*, 24(5), 417-423. <https://doi.org/10.1080/01490450701436505>

[10] Xu, W., Zheng, J., Cui, M., & Lai, H. (2025). Enzyme-Induced Carbonate Precipitation for the Stabilization of Heavy Metal-Contaminated Landfill Soils: A Sustainable Approach to Resource Recovery and Environmental Remediation. *Sustainability*, 17(10), 4630. <https://doi.org/10.3390/su17104630>

[11] Taharia, M., Dey, D., Das, K., Sukul, U., Chen, J.-S., Banerjee, P., Dey, G., Sharma, R. K., Lin, P.-Y., & Chen, C.-Y. (2024). Microbial induced carbonate precipitation for remediation of heavy metals, ions and radioactive elements: A comprehensive exploration of prospective applications in water and soil treatment. *Ecotoxicology and Environmental Safety*, 271, 115990. <https://doi.org/10.1016/j.ecoenv.2024.115990>

[12] Torres-Aravena, Á. E., Duarte-Nass, C., Azócar, L., Mella-Herrera, R., Rivas, M., & Jeison, D. (2018). Can Microbially Induced Calcite Precipitation (MICP) through a Ureolytic Pathway Be Successfully Applied for Removing Heavy Metals from Wastewaters? *Crystals*, 8(11), 438. <https://doi.org/10.3390/cryst8110438>

- [13] Brazier, J.-M., Goetschl, K.E., Dietzel, M. and Mavromatis, V., 2024. Effect of mineral growth rate on zinc incorporation into calcite and aragonite. *Chemical Geology*, 643, 121821. <https://doi.org/10.1016/j.chemgeo.2023.121821>
- [14] Zeng, H., Jin, B., Xu, S., Han, L., Wang, J., Jia, H., Dapaah, M.F. & Cheng, L. (2025) Removal of copper, lead and cadmium from water through enzyme-induced carbonate precipitation by soybean urease. *Environ Res*, 277, 121610. <https://doi.org/10.1016/j.envres.2025.121610>
- [15] Gomez, M.G., Martinez, B.C., DeJong, J.T., Hunt, C.E., deVlaming, L.A., Major, D.W. & Dworatzek, S.M. (2015) Field-scale bio-cementation tests to improve sands. *Proceedings of the Institution of Civil Engineers – Ground Improvement*, 168(3), 206–216. <https://doi.org/10.1680/grim.13.00052>
- [16] Almajed, A., Abbas, H., Arab, M., Alsabhan, A., Hamid, W. & Al-Salloum, Y. (2020) Enzyme-induced carbonate precipitation (EICP)-based methods for ecofriendly stabilization of different types of natural sands. *Journal of Cleaner Production*, 274, 122627. <https://doi.org/10.1016/j.jclepro.2020.122627>
- [17] Arab, M.G., Alsodi, R., Almajed, A., Yasuhara, H., Zeiada, W. & Shahin, M.A. (2021) State-of-the-art review of enzyme-induced calcite precipitation (EICP) for ground improvement: applications and prospects. *Geosciences*, 11, 492. <https://doi.org/10.3390/geosciences11120492>
- [18] Moghal, A.A.B., Lateef, M.A., Mohammed, S.A., Ahmad, M., Usman, A.R.A. & Almajed, A. (2020) Heavy metal immobilization studies and enhancement in geotechnical properties of cohesive soils by EICP technique. *Applied Sciences*, 10, 7568. <https://doi.org/10.3390/app10217568>
- [19] Makinda, J., Kassim, K.A., Muhammed, A.S., Zango, M.U. & Gungat, L. (2023) Immobilization of heavy metal contaminants in mining waste through enzyme-induced calcite precipitation biocementation. *E3S Web of Conferences*, 464, 07001.
- [20] Proudfoot, D., Brooks, L., Gammons, C.H., Barth, E., Bless, D., Nagisetty, R.M. & Lauchnor, E.G. (2022) Investigating the potential for microbially induced carbonate precipitation to treat mine waste. *J Hazard Mater*, 424(Pt C), 127490. <https://doi.org/10.1016/j.jhazmat.2021.127490>
- [21] Behera, S.N., Sharma, M., Aneja, V.P. & Balasubramanian, R. (2013) Ammonia in the atmosphere: a review on emission sources, atmospheric chemistry and deposition on terrestrial bodies. *Environmental Science and Pollution Research*, 20(11), 8092–8131. <https://doi.org/10.1007/s11356-013-2051-9>
- [22] Park, J., Kim, E., Oh, S., Kim, H., Kim, S., Kim, Y.P. & Song, M. (2021) Contributions of ammonia to high concentrations of PM_{2.5} in an urban area. *Atmosphere*, 12(12), 1676. <https://doi.org/10.3390/atmos12121676>
- [23] Gowthaman, S., Mohsenzadeh, A., Nakashima, K. & Kawasaki, S. (2022) Removal of ammonium by-products from the effluent of bio-cementation system through struvite precipitation. *Materials Today: Proceedings*, 61(Part 2), 243–249. <https://doi.org/10.1016/j.matpr.2021.09.013>
- [24] Farghali, M., Chen, Z., Osman, A.I. et al. (2024) Strategies for ammonia recovery from wastewater: a review. *Environmental Chemistry Letters*, 22, 2699–2751. <https://doi.org/10.1007/s10311-024-01768-6>
- [25] Su, F., Yang, Y., Qi, Y. & Zhang, H. (2022) Combining microbially induced calcite precipitation (MICP) with zeolite: A new technique to reduce ammonia emission and enhance soil treatment

ability of MICP technology. *J Environ Chem Eng*, 10(3), 107770. <https://doi.org/10.1016/j.jece.2022.107770>

[26] Hanisch, P., Pechtl, M., Maurer, H., Maier, F., Bischof, S., Nagy, B., Eulenkamp, C., Kustermann, A. & Huber, R. (2024) The effect of different additives on bacteria adsorption, compressive strength and ammonia removal for MICP. *Environ Earth Sci*, 83, 635. <https://doi.org/10.1007/s12665-024-11929-z>

[27] Liu, Y., Li, J., Su, J., Li, X. & Li, X. (2024) Simultaneous removal of ammonia nitrogen, calcium and cadmium in a biofilm reactor based on microbial-induced calcium precipitation: Optimization of conditions, mechanism and community biological response. *J Environ Manage*, 358, 120912. <https://doi.org/10.1016/j.jenvman.2024.120912>

[28] Jiang, L., Liu, X., Yin, H., Liang, Y., Liu, H., Miao, B., Peng, Q., Meng, D., Wang, S., Yang, J. & Guo, Z. (2020) The utilization of biomineralization technique based on microbial induced phosphate precipitation in remediation of potentially toxic ions contaminated soil: a mini review. *Ecotoxicology and Environmental Safety*, 191, 110009. <https://doi.org/10.1016/j.ecoenv.2019.110009>

[29] Han, L.-J., Li, J.-S., Xue, Q., Guo, M.-Z., Wang, P. & Poon, C.S. (2022) Enzymatically induced phosphate precipitation (EIPP) for stabilization/solidification (S/S) treatment of heavy metal tailings. *Construction and Building Materials*, 314(Part A), 125577. <https://doi.org/10.1016/j.conbuildmat.2021.125577>

[30] Lai, H., Ding, X., Cui, M., Zheng, J., Chen, Z., Pei, J. & Zhang, J. (2023) Mechanisms and influencing factors of biomineralization-based heavy metal remediation: a review. *Biogeotechnics*, 1(3), 100039. <https://doi.org/10.1016/j.bgtech.2023.100039>

[31] Gowthaman, S., Yamamoto, M., Chen, M., Nakashima, K. & Kawasaki, S. (2023) Baseline investigation on enzyme induced calcium phosphate precipitation for solidification of sand. *Frontiers in Built Environment*, 9. <https://doi.org/10.3389/fbuil.2023.1307650>

[32] Cao, R.X., Ma, L.Q., Chen, M., Singh, S.P. & Harris, W.G. (2003) Phosphate-induced metal immobilization in a contaminated site. *Environmental Pollution*, 122(1), 19–28. [https://doi.org/10.1016/S0269-7491\(02\)00283-X](https://doi.org/10.1016/S0269-7491(02)00283-X)

[33] Xu, Y. & Schwartz, F.W. (1994) Lead immobilization by hydroxyapatite in aqueous solutions. *Journal of Contaminant Hydrology*, 15(3), 187–206. [https://doi.org/10.1016/0169-7722\(94\)90024-8](https://doi.org/10.1016/0169-7722(94)90024-8)

[34] Ma, Q.Y., Logan, T.J. & Traina, S.J. (1995) Lead immobilization from aqueous solutions and contaminated soils using phosphate rocks. *Environmental Science & Technology*, 29(4), 1118–1126. <https://doi.org/10.1021/es00004a034>

[35] Li, X., Azimzadeh, B., Martinez, C.E. & McBride, M.B. (2021) Pb mineral precipitation in solutions of sulfate, carbonate and phosphate: measured and modeled Pb^{2+} solubility and Pb^{2+} activity. *Minerals*, 11(6), 620. <https://doi.org/10.3390/min11060620>

[36] Ryan, J.A., Zhang, P., Hesterberg, D., Chou, J. & Sayers, D.E. (2001) Formation of chloropyromorphite in a lead-contaminated soil amended with hydroxyapatite. *Environmental Science & Technology*, 35(18), 3798–3803. <https://doi.org/10.1021/es010634l>

- [37] Liu, D., Li, Z., Li, W., Zhong, Z., Xu, J., Ren, J. & Ma, Z. (2013) Adsorption behavior of heavy metal ions from aqueous solution by soy protein hollow microspheres. *Industrial & Engineering Chemistry Research*, 52(32), 11036–11044. <https://doi.org/10.1021/ie401092f>
- [38] Mejáre, M. & Bülow, L. (2001) Metal-binding proteins and peptides in bioremediation and phytoremediation of heavy metals. *Trends in Biotechnology*, 19(2), 67–73.
- [39] Reddy, G.N. & Prasad, M.N.V. (1990) Heavy metal-binding proteins/peptides: occurrence, structure, synthesis and functions. A review. *Environmental and Experimental Botany*, 30(3), 251–264. [https://doi.org/10.1016/0098-8472\(90\)90024-Z](https://doi.org/10.1016/0098-8472(90)90024-Z)
- [40] Luo, Y., Zhang, Y., Xiong, Z., Chen, X., Sha, A., Xiao, W., Peng, L., Zou, L., Han, J. & Li, Q. (2024) Peptides used for heavy metal remediation: a promising approach. *International Journal of Molecular Sciences*, 25, 6717. <https://doi.org/10.3390/ijms25126717>
- [41] Hendriks, W. H., Butts, C. A., Thomas, D. V., James, K. A. C., Morel, P. C. A., & Versteegen, M. W. A. (2002). Nutritional quality and variation of meat and bone meal. *Asian-Australasian Journal of Animal Sciences*, 15(10), 1507–1516. <https://doi.org/10.5713/ajas.2002.1507>
- [42] Ajsuvakova, O.P., Tinkov, A.A., Aschner, M., Rocha, J.B.T., Michalke, B., Skalnaya, M.G., Skalny, A.V., Butnariu, M., Dadar, M., Sarac, I., Aaseth, J. & Bjørklund, G. (2020) Sulfhydryl groups as targets of mercury toxicity. *Coordination Chemistry Reviews*, 417, 213343. <https://doi.org/10.1016/j.ccr.2020.213343>
- [43] Bjørklund, G., Crisponi, G., Nurchi, V.M., Cappai, R., Djordjevic, A.B. & Aaseth, J. (2019) A review on coordination properties of thiol-containing chelating agents towards mercury, cadmium, and lead. *Molecules*, 24(18), 3247. <https://doi.org/10.3390/molecules2418324>
- [44] Yang, X., Wan, Y., Zheng, Y., He, F., Yue, Z., Huang, J., Wang, H., Ok, Y.S., Jiang, Y. & Gao, B. (2019) Surface functional groups of carbon-based adsorbents and their roles in the removal of heavy metals from aqueous solutions: a critical review. *Chemical Engineering Journal*, 366, 608–621. <https://doi.org/10.1016/j.cej.2019.02.119>
- [45] Bulgariu, L., Ferțu, D.I., Cara, I.G. & Gavrilăscu, M. (2021) Efficacy of alkaline-treated soy waste biomass for the removal of heavy-metal ions and opportunities for their recovery. *Materials*, 14(23), 7413. <https://doi.org/10.3390/ma14237413>
- [46] Vandenbossche, M., Jimenez, M., Casetta, M., & Traisnel, M. (2015). Remediation of Heavy Metals by Biomolecules: A Review. *Critical Reviews in Environmental Science and Technology*, 45(15), 1644–1704. <https://doi.org/10.1080/10643389.2014.966425>
- [47] Singh, N.A. (2017) Biomolecules for removal of heavy metal. *Recent Patents on Biotechnology*, 11(3), 197–203. <https://doi.org/10.2174/1872208311666170223155019>
- [48] Wen, X., Du, Q., & Tang, H. (1998). *Surface complexation model for the sorption of rare earth elements on oxide minerals*. *Environmental Science & Technology*, 32(7), 870–875. <https://doi.org/10.1021/es970098q>
- [49] Raji, Z.; Karim, A.; Karam, A.; Khalloufi, S. Adsorption of Heavy Metals: Mechanisms, Kinetics, and Applications of Various Adsorbents in Wastewater Remediation—A Review. *Waste* 2023, 1, 775–805. <https://doi.org/10.3390/waste1030046>

- [50] Uddin, M. K. (2017). A review on the adsorption of heavy metals by clay minerals, with special focus on the past decade. *Chemical Engineering Journal*, 308, 438–462. <https://doi.org/10.1016/j.cej.2016.09.029>
- [51] Li, Y., Zhao, X., Wu, J., & Gu, X. (2020). Surface complexation modeling of divalent metal cation adsorption on birnessite. *Chemical Geology*, 551, 11977
- [52] Tang, S., Dong, Z., Ke, X., Luo, J. & Li, J. (2021) Advances in biomineralization-inspired materials for hard tissue repair. *International Journal of Oral Science*, 13(1), 42. <https://doi.org/10.1038/s41368-021-00134-1>
- [53] Weiner, S. & Addadi, L. (2011) Crystallization pathways in biomineralization. *Annual Review of Materials Research*, 41, 21–40. <https://doi.org/10.1146/annurev-matsci-062910-095803>
- [54] Hu, H., Lin, Y., Yang, B., Wen, X., Ma, P., Loh, X. J., Luo, Z., Li, Z., & Wu, Y.-L. (2025). Biomineralization-inspired functional biomaterials: From principles to practice. *Chemical Engineering Journal*, 504, 158624. <https://doi.org/10.1016/j.cej.2024.158624>
- [55] Wang, Q., Hu, L., Wang, X., & Tang, R. (2024). Expanding from materials to biology inspired by biomineralization. *Interdisciplinary Materials*, 3(1), e12144. <https://doi.org/10.1002/idm2.12144>
- [56] De Yoreo, J. J. (2010). Physical mechanisms of crystal growth modification by biomolecules. *AIP Conference Proceedings*, 1270(1), 45–58. <https://doi.org/10.1063/1.3476238>
- [57] Gebauer, D. et al. (2014) Pre-nucleation clusters as solute precursors in crystallisation. *Chemical Society Reviews*, 43(7), 2348–2371.
- [58] Lu, C.-G., Jiao, C.-J., Zhang, X.-C., Zheng, J.-S., & Chen, X.-F. (2025). Advancements in the research on the preparation and growth mechanisms of various polymorphs of calcium carbonate: A comprehensive review. *Crystals*, 15(3), 265. <https://doi.org/10.3390/cryst15030265>
- [59] Jin, B., Ma, H., Hart, A., et al. (2021). Real-time observation of the transformation of amorphous calcium phosphate to hydroxyapatite. *Nature Communications*, 12, 5487. <https://doi.org/10.1038/s41467-021-25679-9>
- [60] Chatzipanagis, K., Persson, I., Björn, E., et al. (2016). Citrate-controlled growth of biomimetic apatite nanocrystals. *CrystEngComm*, 18(5), 626–635. <https://doi.org/10.1039/C5CE01793G>
- [61] Ashokan, A., Sampath Kumar, T. S., & Jayaraman, G. (2022). Process optimization for the rapid conversion of calcite into hydroxyapatite microspheres for chromatographic applications. *Scientific Reports*, 12, Article 12164. <https://doi.org/10.1038/s41598-022-16163-y>
- [62] Whiffin, V. S. (2004). *Microbial CaCO₃ precipitation for the production of biocement* (PhD thesis). Murdoch University, Perth, Western Australia.
- [63] Saif, A., Cuccurullo, A., Gallipoli, D., Perlot, C., & Bruno, A. W. (2022). Advances in enzyme induced carbonate precipitation and application to soil improvement: A review. *Materials*, 15(3), 950. <https://doi.org/10.3390/ma15030950>
- [64] Wang, Y., Sun, X., Miao, L., Wang, H., Wu, L., Shi, W., & Kawasaki, S. (2024). State-of-the-art review of soil erosion control by MICP and EICP techniques: Problems,

applications, and prospects. *Science of The Total Environment*, 912, 169016. <https://doi.org/10.1016/j.scitotenv.2023.169016>

[65] Stocks-Fischer, S., Galinat, J.K. & Bang, S.S. (1999) Microbiological precipitation of CaCO₃. *Soil Biology and Biochemistry*, 31, 1563–1571.

[66] Xiao, J., Huang, J., Jiang, Y., Chong, C., Zhang, L., & Zhang, X. (2017). Comparison analysis of dust-depressor using microbial induced carbonate precipitation with urease reagent. *Sustainability in Environment*, 2(4), 379–393. <https://doi.org/10.22158/se.v2n4p379>

[67] Shu, S., Yan, B., Ge, B., Li, S., & Meng, H. (2022). Factors affecting soybean crude urease extraction and biocementation via enzyme-induced carbonate precipitation (EICP) for soil improvement. *Energies*, 15(15), 5566. <https://doi.org/10.3390/en15155566>

[68] Beaufiles, C., Man, H.-M., de Poulpiquet, A., Mazurenko, I. & Lojou, E. (2021) From enzyme stability to enzymatic bioelectrode stabilization processes. *Catalysts*, 11(4), 497. <https://doi.org/10.3390/catal11040497>

[69] Bulgariu, L., & Bulgariu, D. (2018). Functionalized soy waste biomass – A novel environmentally friendly biosorbent for the removal of heavy metals from aqueous solution. *Journal of Cleaner Production*, 197(Part 1), 875–885. <https://doi.org/10.1016/j.jclepro.2018.06.261>

[70] Lin, J., Chen, N., & Pan, Y. (2013). Arsenic incorporation in synthetic struvite (NH₄MgPO₄·6H₂O): a synchrotron XAS and single-crystal EPR study. *Environmental science & technology*, 47(22), 12728–12735. <https://doi.org/10.1021/es402710y>

[71] Horak, M., Hic, P., Balik, J., & Koziskova, J. (2021). Arsenic as a contaminant of struvite when recovering phosphorus from phosphogypsum wastewater. *Journal of the Taiwan Institute of Chemical Engineers*, 129, 91–96. <https://doi.org/10.1016/j.jtice.2021.10.005>

[72] Zaborska, W., Krajewska, B., & Olech, Z. (2004). Heavy Metal Ions Inhibition of Jack Bean Urease: Potential for Rapid Contaminant Probing. *Journal of Enzyme Inhibition and Medicinal Chemistry*, 19(1), 65–69. <https://doi.org/10.1080/14756360310001650237>

[73] Krajewska, B. (2009). Ureasases I. Functional, catalytic and kinetic properties: A review. *Journal of Molecular Catalysis B: Enzymatic*, 59(1–3), 9–21. <https://doi.org/10.1016/j.molcatb.2009.01.003>

[74] Spuches, A. M., Kruszyna, H. G., Rich, A. M., & Wilcox, D. E. (2005). Thermodynamics of the As(III)–Thiol Interaction: Arsenite and monomethylarsenite complexes with glutathione, dihydrolipoic acid, and other thiol ligands. *Inorganic Chemistry*, 44(8), 2964–2972. <https://doi.org/10.1021/ic048694q>

[75] Rouff, A. A., Ma, N., & Kustka, A. B. (2016). Adsorption of arsenic with struvite and hydroxylapatite in phosphate-bearing solutions. *Chemosphere*, 146, 574–581. <https://doi.org/10.1016/j.chemosphere.2015.12.061>

[76] Goldberg, S., & Johnston, C. T. (2001). Mechanisms of arsenic adsorption on amorphous oxides evaluated using macroscopic measurements, vibrational spectroscopy, and surface complexation modeling. *Journal of Colloid and Interface Science*, 234(1), 204–216. <https://doi.org/10.1006/jcis.2000.7295>

- [77] Jain, A. and Loeppert, R.H. (2000), Effect of Competing Anions on the Adsorption of Arsenate and Arsenite by Ferrihydrite. *Journal of Environmental Quality*, 29: 1422-1430. <https://doi.org/10.2134/jeq2000.00472425002900050008x>
- [78] Vergara-Gerónimo, B., Ávila-Acevedo, G., Riverón-Negrete, L., Guevara, J., & Salas-Luis, M. A. (2021). Arsenic-protein interactions as a mechanism of arsenic toxicity. *Toxicology Mechanisms and Methods*, 31(4), 249-260. <https://doi.org/10.1080/15376516.2021.1903785>
- [79] Ramírez-Solís, A., Mukopadhyay, R., Rosen, B. P., & Stemmler, T. L. (2004). Experimental and theoretical characterization of arsenite in water: insights into the coordination environment of As-O. *Inorganic chemistry*, 43(9), 2954-2959. <https://doi.org/10.1021/ic0351592>
- [80] Krajewska, B. (2008). Mono- (Ag, Hg) and di- (Cu, Hg) valent metal ions effects on the activity of jack bean urease. Probing the modes of metal binding to the enzyme. *Journal of Enzyme Inhibition and Medicinal Chemistry*, 23(4), 535-542. <https://doi.org/10.1080/14756360701743051>
- [81] Madsen, H. E. L. (2005). Crystal growth kinetics of copper phosphate from acid solution at 37 °C. *Journal of Crystal Growth*, 275(1-2), e191-e196. <https://doi.org/10.1016/j.jcrysgro.2004.10.140>
- [82] Cudennec, Y., & Lecerf, A. (2003). The transformation of Cu(OH)₂ into CuO, revisited. *Solid State Sciences*, 5(11-12), 1471-1474. <https://doi.org/10.1016/j.solidstatesciences.2003.09.009>
- [83] Gadd, G.M. (2010) Metals, minerals and microbes: geomicrobiology and bioremediation. *Microbiology*, 156(3), 609-643. DOI: 10.1099/mic.0.037143-0
- [84] Shannon, R.D. (1976) Revised effective ionic radii and systematic studies of interatomic distances in halides and chalcogenides. *Acta Crystallographica Section A*, 32(5), 751-767.
- [85] Fenter, P., & Sturchio, N. C. (2004). Mineral-water interfacial structures revealed by synchrotron X-ray scattering. *Progress in Surface Science*, 77(5-8), 171-258. <https://doi.org/10.1016/j.progsurf.2004.12.001>
- [86] Fang, Z., Liu, W., Yao, T., Zhou, G., Wei, S. & Qin, L. (2022) Experimental study of chromium (III) coprecipitation with calcium carbonate. *Geochimica et Cosmochimica Acta*, 322, 94-108. <https://doi.org/10.1016/j.gca.2022.02.010>
- [87] Rouff, A.A. (2012) Sorption of chromium with struvite during phosphorus recovery. *Environmental Science & Technology*, 46(22), 12493-12501. <https://doi.org/10.1021/es302296m>
- [88] Tang, C., Liu, Z., Peng, C., Chai, L.-Y., Kuroda, K., Okido, M. & Song, Y.-X. (2019) New insights into the interaction between heavy metals and struvite: struvite as platform for heterogeneous nucleation of heavy metal hydroxide. *Chemical Engineering Journal*, 365, 60-69. <https://doi.org/10.1016/j.cej.2019.02.034>
- [89] Tabatabai, M. A., & Bremner, J. M. (1972). Assay of urease activity in soils. *Soil Biology and Biochemistry*, 4(4), 479-487. [https://doi.org/10.1016/0038-0717\(72\)90064-8](https://doi.org/10.1016/0038-0717(72)90064-8)
- [90] Zhu, M., Ginder-Vogel, M., & Sparks, D. L. (2010). Ni(II) sorption on biogenic Mn-oxides with varying Mn octahedral layer structure. *Environmental science & technology*, 44(12), 4472-4478. <https://doi.org/10.1021/es9037066>

- [91] Lakshtanov, L. Z., & Stipp, S. L. S. (2007). Experimental study of nickel(II) interaction with calcite: Adsorption and coprecipitation. *Geochimica et Cosmochimica Acta*, 71(15), 3686–3697. <https://doi.org/10.1016/j.gca.2007.05.001>
- [92] Elzinga, E. J., & Reeder, R. J. (2002). X-ray absorption spectroscopy study of Cu^{2+} and Zn^{2+} adsorption complexes at the calcite surface: Implications for site-specific metal incorporation preferences during calcite crystal growth. *Geochimica et Cosmochimica Acta*, 66(22), 3943–3954. [https://doi.org/10.1016/S0016-7037\(02\)00971-7](https://doi.org/10.1016/S0016-7037(02)00971-7)
- [93] Hövelmann, J., Stawski, T. M., Freeman, H. M., Besselink, R., Mayanna, S., Perez, J. P. H., Hondow, N. S., & Benning, L. G. (2019). *Struvite crystallisation and the effect of Co^{2+} ions*. *Minerals*, 9(8), 495. <https://doi.org/10.3390/min9080495>
- [94] Kubier, A., Wilkin, R. T., & Pichler, T. (2019). Cadmium in soils and groundwater: A review. *Applied geochemistry : journal of the International Association of Geochemistry and Cosmochemistry*, 108, 1–16. <https://doi.org/10.1016/j.apgeochem.2019.104388>
- [95] Liu, H., Lu, X., Cui, X., Zhang, L., & Chan, T.-S. (2022). Atomistic mechanism of cadmium incorporation into hydroxyapatite. *American Mineralogist*, 107(4), 664–672. <https://doi.org/10.2138/am-2020-7560>
- [96] Lu, X., Li, J., Xu, W., Qi, Z., & Wang, F. (2024). Co-precipitation of Cd with struvite during phosphorus recovery. *Chemosphere*, 346, 140610. <https://doi.org/10.1016/j.chemosphere.2023.140610>
- [97] Sasamoto, R., Kanda, Y., & Yamanaka, S. (2022). Difference in cadmium chemisorption on calcite and vaterite porous particles. *Chemosphere*, 297, 134057. <https://doi.org/10.1016/j.chemosphere.2022.134057>
- [98] Dudev, T., & Lim, C. (2011). Competition between Li^+ and Mg^{2+} in metalloproteins: Implications for lithium therapy. *Journal of the American Chemical Society*, 133(23), 9506–9515. <https://doi.org/10.1021/ja201985s>
- [99] Föger, A., Konrad, F., Leis, A., Dietzel, M., & Mavromatis, V. (2019) Effect of growth rate and pH on lithium incorporation in calcite. *Geochimica et Cosmochimica Acta*, 248, 14–24. <https://doi.org/10.1016/j.gca.2018.12.040>
- [100] Pastero, L., Costa, E., Bruno, M., Rubbo, M., Sgualdino, G., & Aquilano, D. (2004). Morphology of calcite (CaCO_3) crystals growing from aqueous solutions in the presence of Li^+ ions: Surface behavior of the {0001} form. *Crystal Growth & Design*, 4(3), 485–490. <https://doi.org/10.1021/cg034217r>
- [101] Gu, K., Feng, W., Wei, H., & Dang, L. (2024). The Factors Influencing Lithium Carbonate Crystallization in Spent Lithium-Ion Battery Leachate. *Processes*, 12(4), 753. <https://doi.org/10.3390/pr12040753>
- [102] Fulfer, K.D., Galle Kankanamge, S.R., Chen, X., Woodard, K.T. & Kuroda, D.G. (2025) Elucidating the mechanism behind the infrared spectral features and dynamics observed in the carbonyl stretch region of organic carbonates interacting with lithium ions. *Journal of Chemical Physics*, [early access]. <https://doi.org/10.1063/5.0049742>

- [103] Rouff, A.A. & Juarez, K.M. (2014) Zinc interaction with struvite during and after mineral formation. *Environmental Science & Technology*, 48(11), 6342–6349. <https://doi.org/10.1021/es500188t>
- [104] Lu, X., Huang, Z., Liang, Z., Li, Z., Yang, J., Wang, Y. & Wang, F. (2021) Co-precipitation of Cu and Zn in precipitation of struvite. *Science of the Total Environment*, 764, 144269. <https://doi.org/10.1016/j.scitotenv.2020.144269>
- [105] Achilleos, P., Roberts, K. R., & Williams, I. D. (2022). Struvite precipitation within wastewater treatment: A problem or a circular economy opportunity?. *Heliyon*, 8(7), e09862. <https://doi.org/10.1016/j.heliyon.2022.e09862>
- [106] Warmadewanthi, J., & Liu, J.C. (2009). Recovery of phosphate and ammonium as struvite from semiconductor wastewater. *Separation and Purification Technology*, 64(3), 368–373. <https://doi.org/10.1016/j.seppur.2008.10.040>
- [107] Sasamoto, R., Kanda, Y. & Yamanaka, S., 2022. *Difference in cadmium chemisorption on calcite and vaterite porous particles*. *Chemosphere*, 297, p.134057. <https://doi.org/10.1016/j.chemosphere.2022.134057>
- [108] Ghizellaoui, S. & Euvrard, M. (2008). *Assessing the effect of zinc on the crystallization of calcium carbonate*. *Desalination*, 220(1–3), pp.394–402. <https://doi.org/10.1016/j.desal.2007.02.044>
- [109] Rouff, A.A. & Juarez, K.M. (2014) Zinc interaction with struvite during and after mineral formation. *Environmental Science & Technology*, 48(11), 6342–6349. <https://doi.org/10.1021/es500188t>
- [110] Warmadewanthi, D. & Liu, J.C. (2009). Recovery of phosphate and ammonium as struvite from semiconductor wastewater. *Separation and Purification Technology*, 64(3), 368–373. <https://doi.org/10.1016/j.seppur.2008.10.040>
- [111] Rivadeneira, M.A., González-López, J. & Ramos-Cormenzana, A. (1985). Influence of ammonium ions on calcite and struvite formation by *Azotobacter* in chemically defined media. *Folia Microbiologica*, 30(1), 55–57. <https://doi.org/10.1007/BF02931430>
- [112] Söhnel, O., Handlířová, M. & Macenauer, J. (1990). Kinetics of growth of calcite crystals in presence of ammonium ions. *Crystal Research and Technology*, 25(12), 1368–1372. <https://doi.org/10.1002/crat.2170251202>
- [113] Zhang, L., Wang, S., Jiao, L., Li, Y., Yang, J., Zhang, R., Feng, S., & Wang, J. (2016). Effects of organic matter content and composition on ammonium adsorption in lake sediments. *Environmental Science and Pollution Research*, 23, 6179–6187. <https://doi.org/10.1007/s11356-015-5820-9>
- [114] Balzano S, Sardo A, Blasio M, Chahine TB, Dell'Anno F, Sansone C and Brunet C (2020) Microalgal Metallothioneins and Phytochelatins and Their Potential Use in Bioremediation. *Front. Microbiol.* 11:517. doi: 10.3389/fmicb.2020.00517
- [115] GHG PROTOCOL. *The Greenhouse Gas Protocol: A Corporate Accounting and Reporting Standard*. Revised Edition. Geneva: World Resources Institute; World Business Council for Sustainable Development, 2004.

